Nanostructured Materials for Electrochemical CO_2 Reduction to Multicarbon Products

by

Joel Philip Mills

A thesis

presented to the University of Waterloo

in fulfilment of the

thesis requirement for the degree of

Master of Applied Science

in

Mechanical and Mechatronics Engineering

Waterloo, Ontario, Canada, 2022

© Joel Philip Mills 2022

Author's Declaration

This thesis consists of material all of which I authored or co-authored: see Statement of Contributions included in the thesis. This is a true copy of the thesis, including any required final revisions, as accepted by my examiners.

I understand that my thesis may be made electronically available to the public.

Statement of Contributions

Joel Mills was the sole author for Chapters 1, 2, 3, 6 and 7 which were written under the supervision of Dr. Yimin Wu and were not written for publication. Joel Mills was the sole author for Chapter 4, which is a revised and expounded version of a work previously submitted to Dr. Mustafa Yavuz prepared under the supervision of Dr. Yimin Wu.

This thesis consists in part of one manuscript written for publication. Exceptions to sole authorship of material are as follows:

Research presented in Chapter 5:

Title: Achieving 94% Faradic efficiency toward multicarbon products in CO_2 electroreduction via synergy between AgCu single-atom alloy and Ag nanoparticles

Authors: Cheng Du, [Δ] Joel. P. Mills, [Δ] Asfaw G. Yohannes,[Δ] Jian-Xiang Lian, Maoyu Wang, Tao Guo, Xiyang Wang, Hua Zhou, Cheng-Jun Sun, John Z. Wen, Brian Kendall, Martin Couillard, Hongsheng Guo, Samira Siahrostami, Yimin A. Wu

Δ Equal contribution

The final version of this manuscript has been submitted for publication.

Y.A.W. conceived and supervised the research. S.S. led the DFT calculations. C.D. and J.P.M carried out the catalyst's synthesis, characterization, and performance test. A.G.Y. and J.X.L conducted the DFT calculations. M.W., H.Z., and C.J.S carried out the XAFS measurements and data fitting. T.G. and X.W. assisted in the materials characterizations. J.Z.W and H.G. provided advice for the research and the analysis of results. B.K. performed ICP test. M.C. measured the TEM experiments. All authors cowrite the manuscript.

As co-lead author of this chapter, I was responsible for contributing to carrying out data collection and analysis and drafting manuscripts. My coauthors provided guidance during each step of the research and provided feedback on draft manuscripts.

Abstract

Electrochemical CO_2 reduction technology offers promise as a method of carbon storage and energy storage in a world where anthropogenic CO_2 levels in the atmosphere are linked with climatic degradation. The main missing piece of an electrochemical CO_2 reduction system is the catalyst. Therefore, there are significant efforts to design effective catalysts to convert CO_2 into useful products. Multicarbon products are targeted for their relatively high commercial value.

In a review of the relevant literature, we present some of the most successful catalyst design strategies for conversion of CO_2 into multicarbon products. Following this, we introduce in detail the catalyst design features implemented in the results portion of this work.

Next, the experimental methods used in this thesis are described. These include the synthesis of catalyst materials, the methods for measuring the performance of these catalysts, and finally the characterization techniques used to describe the catalysts. The material characterization provides information used to understand their performance.

The fourth chapter comprises a high-level view of the economics of CO_2 conversion. This analysis informs the areas of focus for researchers, with the ultimate goal of making CO_2 conversion a profitable venture.

This is followed by a complete experimental work presenting a novel, high-performance catalyst, entitled *Achieving 94% Faradic Efficiency toward Multicarbon Products in CO_2 Electroreduction via Synergy Between AgCu Single-Atom Alloy and Ag Nanoparticles*. The material is characterized comprehensively, and the catalytic performance is explained using theoretical calculations from collaborators.

The following chapter consists of the initial stages of a second experimental work based on another catalyst material. The catalyst is a high-entropy alloy with potential for CO_2 conversion performance. Following synthesis and characterization details, the next steps for this work are detailed.

Finally, we summarize conclusions of this work and discuss new directions for this research area.

Acknowledgements

First and foremost, I would like to acknowledge my supervisor, Dr. Yimin A. Wu, for his deep expertise and knowledge, consistent support of me, encouragement, and understanding. It cannot recall ever waiting more than a few minutes after requesting assistance to receive a reply. Thank you for being there for me.

My fellow members of our research group, the Materials Interface Foundry have furnished me with examples to follow, advice, friendship, and knowledge. Specifically, I would like to thank Dr. Cheng Du, who spent countless hours teaching me the fundamentals of running experiments and producing impactful research. I would also like to thank Zuolong (Jeffrey) Chen, Lei (Ray) Wang, Wei Wei and Dr. Xiyang Wang.

I would also like to thank my great roommates over the course of my degree, Ian Lung, Hailey Reynolds, and Jake Welfare, who graciously supported me during the pleasant and difficult parts of this adventure.

I am grateful to my thesis readers, Dr. Xianguo Li and Dr. Mustafa Yavuz, for their time spent reading my thesis and offering their feedback.

I would like to recognize the support from the National Research Council of Canada's (NRC) Materials for Clean Fuels Challenge program. While working on a project under this program I was fortunate to receive support from Dr. Martin Couillard and Dr. Hongsheng Guo, specifically with material characterization, and in the general progression along the goals of the program.

Finally, I would like to thank my parents and siblings for their support and for believing in me: Peter, Patricia, Laura, and Timothy Mills.

Table of Contents

Author's Declaration ii

Statement of Contributions iii

Abstract iv

Acknowledgements v

List of Figures ix

List of Tables x

List of Abbreviations xi

1. Introduction 1

1.1. The Significance of CO2 Reduction 1

1.2. Components of CO_2 Reduction System, Reaction Products 2

1.3. Requirements of Electrocatalytic CO_2 Reduction: Current Density, Selectivity, Energy Efficiency, and Stability 4

2. Literature Review 6

2.1. Strategies for Carbon-Carbon Coupling 6

2.1.1. Compound-Derived Copper 7

2.1.2. Interfaces 8

2.1.3. Alloying and Doping 8

2.1.4. Metal Organic Frameworks 9

2.2. Catalyst Features Relevant to the Works in this Thesis 11

2.2.1. Single Atom Catalysts 11

2.2.2. High-Entropy Alloys 11

3. Methods 13

3.1. Synthesis Techniques 13

3.1.1. Galvanic replacement 13

3.1.2. Electro-Shock High-Entropy Alloy Synthesis 13

3.2. Performance Testing 14
3.2.1. Electrochemical Cell 14
3.2.2. Electrochemical Control and Measurement 16
3.2.3. Quantifying Gas Products – Gas Chromatography 16
3.2.4. Quantifying Liquid Products – Nuclear Magnetic Resonance Spectroscopy 18
3.3. Material Characterization 19
3.3.1. Microscopy 19
3.3.2. X-Ray Diffraction 19
3.3.3. Inductively Coupled Plasma Mass Spectrometry 19
3.3.4. X-ray Photoelectron Spectroscopy 20
3.3.5. Synchrotron X-Ray Absorption Spectroscopy 20
4. Technoeconomic Analysis: Evaluating the Economic Viability of Electrochemical CO_2 Conversion to Methane 21
4.1. Abstract 21
4.2. Introduction 22
4.3. Electrochemical CO_2 Conversion 23
4.4. Determining Costs 24
4.4.1. Electrical Power Input 25
4.4.2. Cost of Carbon Dioxide 26
4.4.3. Capital Expenditures 27
4.5. Conclusions 28
5. Achieving 94% Faradic efficiency toward multicarbon products in CO_2 electroreduction via synergy between AgCu single-atom alloy and Ag nanoparticles 29
5.1. Abstract 29
5.2. Main 30
5.2.1. Characterization of Catalysts 31

5.2.2. Performance of CO_2 reduction and CO reduction on the catalyst 34
5.2.3. Mechanistic study using density functional theory calculations 37
5.2.4. Ethanol, ethylene, and acetic acid pathways 39
5.2.5. Conclusions 40
5.2.6. Methods 40
5.2.7. Acknowledgment 44
5.3. Supporting Information 45
6. Synthesizing High-Entropy Alloys for Electrochemical CO_2 Conversion 63
6.1. Introduction 63
6.2. Catalyst Synthesis 64
6.3. Results and Discussion 65
6.4. Next Steps 67
7. Conclusions 68
7.1. Main Takeaways from this Work 68
7.2. Future directions 69
8. References 71

List of Figures

All figures are listed here except those appearing in the Supporting Information section 5.3.

Figure 1. Three-chamber flow cell. 15

Figure 2. Devices used for performance testing. (A) Front and (B) top views of Agilent gas chromatograph. (C) Bruker NMR spectrometer and (D) Gamry electrochemical workstation. 17

Figure 3. Scanning transmission electron microscopy imaging of catalysts. (A) Scheme of the synthesis process of AgCu catalysts; (B) BF-STEM image of AgCu SANP; (C) HAADF-STEM image of AgCu SANP; (D) AC-HAADF-STEM image of AgCu SANP; (E) STEM and EDS element mapping images of AgCu SANP. 32

Figure 4. X-ray diffraction and spectroscopies characterization of catalysts. (A) XRD spectra, (B) Ag 3d core-level XPS spectra, (C) Cu 2p core-level XPS spectra of Cu NP, AgCu SAA, AgCu SANP, and AgCu NP; (D) Ag K-edge XANES spectra of AgCu SANP and Ag foil; (E) Ag K-edge XAFS experimental and fitting spectrum of AgCu SANP; (F) Scheme of AgCu SANP structure and the ratio of Ag-Cu and Ag-Ag contribution from fitting results. 33

Figure 5. Electrocatalytic CO2 reduction and CO reduction performance of the catalysts. (A) Scheme of the cascade catalysis mechanism over AgCu SANP; (B) FE results of Cu NP, AgCu SAA, AgCu SANP, and Ag NP catalysts toward CO2RR at -0.65V; (C) Total current density of Cu NP, AgCu SAA, AgCu SANP, and Ag NP catalysts at -0.65V; (D) Performance comparison of AgCu SANP and reported results; (E) FE results of Cu NP, AgCu SAA and AgCu SANP toward CO reduction; (F) Long-term stability results of AgCu SANP toward CO2RR; (G) FE results of AgCu SANP toward CO2RR feeding with different CO2 concentrations. 35

Figure 6. Mechanistic studies by the density functional theory calculations. (A) Comparison of the C-C coupling activation barrier for the *CHO and *COH intermediates; (B) the lowest free energy pathway for the formation of ethanol (orange), ethylene (blue), and acetic acid (magenta), and (C) the associated chemical formula for each elementary step. 38

Figure 7. Scanning electron microscope images (left) and corresponding elemental mapping (right) of selected high-entropy alloy samples. Constituent elements are labelled on each image..... 66

List of Tables

All tables are listed here except those appearing in the Supporting Information section 5.3.

Table 1. Commonly observed products from electrochemical CO_2 reduction. 3

Table 2 Voltages needed for the reactions to proceed, in theory and in practice 25

List of Abbreviations

DFT: density functional theory

ECO_2RR: electrochemical CO_2 reduction reaction

EDX: energy dispersive X-ray spectroscopy

EELS: electron energy loss spectroscopy

FE: faradaic efficiency

CG: gas chromatography

GDE: gas diffusion electrode

HAADF-STEM: high angle angular dark-field scanning transmission electron microscopy

MEA: membrane electrode assembly

NMR: nuclear magnetic resonance spectroscopy

RHE: reversible hydrogen electrode

SEM: scanning electron microscopy

SHE: standard hydrogen electrode

TEM: transmission electron microscopy

XAS: X-ray absorption spectroscopy

XPS: X-ray photoelectron spectroscopy

Chapter 1

1. Introduction

1.1. The Significance of CO_2 Reduction

Given the world's dependence on fossil fuel-based energy sources and their environmental effects, CO_2 conversion into fuels and chemical feedstocks using electrocatalysis is deserving of investment and research effort for the following reasons.

Firstly, CO_2 conversion fills the downstream utilization gap for carbon capture technology. Carbon capture technology, which includes low-concentration direct air capture and high-concentration capture at emission sources, is accepted as a necessary technology for lowering and even maintaining present CO_2 levels, considering the difficulty of completely eliminating the use of fossil fuels. The downstream utilization gap refers to the lack of destinations for this captured carbon. Currently implemented technologies include carbon storage methods which output little to nothing of value; namely mineralization [1] and pumping CO_2 underground. This set of technologies is referred to as carbon capture and storage (CCS).

Enter carbon utilization, expanding the acronym to CCUS. It is hoped that the production of high-value commodity fuels and feedstocks using low-cost renewable electricity can offset the cost of the preceding carbon capture steps [2], easing the economic burden of adopting carbon capture technology.

Filling the downstream carbon utilization gap is not the only synergistic role to be played by CO_2 conversion. With the impending transition away from fossil fuel energy sources towards inherently intermittent renewable energy sources, the technology provides a method to store large quantities of energy, especially for those sources which are seasonally variable, e.g. solar energy collected during summer converted to fuel for use in winter [3]. This form of energy storage is notably compatible with today's existing liquid fuel infrastructure, enabling carbon-neutral energy consumption in existing machines and in the most remote locations.

Carbon-negative sequestration is also possible. If not converted into fuels, the CO_2 can be converted into various chemical feedstocks. One possible destination is plastics, polyethylene via ethylene, for example.

1.2. Components of CO_2 Reduction System, Reaction Products

Electrochemical CO_2 conversion, as the name suggests, depends on electrochemistry. The major components of a system resemble batteries and fuel cells. There are two electrodes, a cathode and an anode, an electrolyte, a membrane, and a power source. These components will now be described in detail.

The cathode, by definition, is the electrode where chemical reduction occurs. This is the location of CO_2 reduction catalysts, the subject of this thesis. CO_2 reduction generally depends on 3 phases to be present at the electrode for successful CO_2 conversion; they are a solid catalyst, a liquid electrolyte (more on this later) and gaseous CO_2. To introduce gaseous CO_2 to the catalyst, state-of-the-art electrodes are designed to allow diffusion of gas through a porous structure to the catalyst and liquid electrolyte. These are called gas diffusion electrodes (GDE). There are significant efforts going into optimising the local environment here, with the goal of maximising CO_2 conversion to desirable products by tuning the surface area, thickness, porosity, and hydrophobicity of GDEs [4].

The anode is the electrode where the other half-reaction takes place. The reaction is generally the oxygen evolution reaction (OER). Although other half-reactions have also been included, like glycerol oxidation, which can lower the required electrical energy input, the relative abundance and low cost of water makes these alternatives much less attractive [5].

The electrolyte solution plays the role of charge carrier in the cell; on the cathode side, the solution also carries the liquid products from the reaction. Aqueous solutions are typically used, with water providing the protons necessary for the reaction. A primary property of the solution is the pH, as proton availability affects the product distribution [6].

The electrochemical system can reduce CO_2 into one of many possible products, or as is almost always the case, a mixture of products.**Table 1** lists the cathode half-reactions most observed in the reduction of CO_2. At the cathode, CO_2 reacts to form a variety of hydrocarbons and oxygenates. In general, larger molecules require more reaction steps and more electrons transferred. For example, ethanol and ethylene require 12 electrons and protons each. The two main implications of this trend are: first, a suitable catalyst must stabilize a longer pathway of intermediates and second, the number of electrons needed to convert one CO_2 molecule increases. This second effect impacts the techno-economics discussed in Chapter 4.

***Table 1**. Commonly observed products from electrochemical CO_2 reduction.*

Product	Equation	Standard potential, E^0
Carbon Monoxide	$CO_2 + 2H^+ + 2e^- \rightleftharpoons CO + H_2O$	-0.11 V
Formic Acid	$CO_2 + 2H^+ + 2e^- \rightleftharpoons CHOOH$	-0.21 V
Methanol	$CO_2 + 6H^+ + 6e^- \rightleftharpoons CH_3OH + H_2O$	-0.03 V
Methane	$CO_2 + 8H^+ + 8e^- \rightleftharpoons CH_4 + 2H_2O$	-0.24 V
Ethylene	$2CO_2 + 12H^+ + 12e^- \rightleftharpoons C_2H_4 + 4H_2O$	-0.07 V
Ethanol	$2CO_2 + 12H^+ + 12e^- \rightleftharpoons C_2H_5OH + 3H_2O$	-0.09 V

1.3. Requirements of Electrocatalytic CO_2 Reduction: Current Density, Selectivity, Energy Efficiency, and Stability

There are a few figures of merit used to compare CO_2 reduction systems. They all impact the economic viability of a proposed system; therefore, they are all included in the technoeconomic analysis.

The first of these figures is current density, which represents the reaction rate per unit area. Current density, j, is measured in A cm^{-2}. To relate this to the amount of product produced, the current is conceptualized as the flow of electrons via Faraday's constant, 96,485 C mol^{-1}, which states that a charge of as many coulombs is carried by one mole of electrons. The ratio of moles electrons passed into a CO_2 reduction product to the moles produced is defined by the relevant chemical equation. In practical terms, the significance of this figure is that a system with a larger current density can divide the capital costs across a larger CO_2 production, all else equal.

The next relevant figure of merit is selectivity, which represents product mixture from the CO_2 conversion system. Selectivity, quantified by Faradaic efficiency or current efficiency, is represented as a percentage. As the name suggests, an understanding of this figure depends on the concepts relating electrical current to product amount produced, as described in the previous paragraph. The figure is defined as the ratio of electrons needed to produce the observed product, divided by the total number of electrons passed through the cell. For example, 70% Faradaic efficiency for ethanol and a 30% Faradaic efficiency for carbon monoxide means that 70% of the electrons contribute to the production of ethanol, while the remaining 30% go into carbon monoxide. Neglecting the charge accumulated in the electrodes, the sum of Faradaic efficiencies for all products always totals to 100%. The electrons must go somewhere. In practical terms, the significance of this figure is that electrons going to undesirable, low-value products are a waste of electrical energy.

Continuing along the line of electrical energy usage, it is important to consider the overall energy efficiency figure. The electrical power consumed by a reactor is the product of the current, mentioned in the last paragraph, and the cell voltage, or potential difference across the cell. In addition to small ohmic losses, the total cell voltage is divided, in series, between the solution and membrane located between the electrodes, and the reactions at the electrodes themselves. The theoretical minimum potential for a cell is the sum of the standard potentials for the two half reactions. Any potential in excess of this is called the overpotential; cells incorporating reference electrodes can accurately quantify overpotential at one electrode by effectively placing a voltmeter between the working electrode and the nearby electrolyte

solution. In addition to this electrical energy input, a holistic approach considers the necessary processes around the reaction. For example, any unreacted CO_2 in the output stream is either waste or needs to be recycled; both options have an impact on the overall energy efficiency. This waste is quantified by carbon efficiency, the fraction of CO_2 which is converted. The exact impact of these losses depends on the performance of the adjacent systems.

Finally, stability is a critical figure. By its nature, it is often the last figure a researcher learns about a newly synthesized material. Adequate performance of a candidate system over the course of a short test is made much less valuable if the system proves to degrade and require component replacement or corrective intervention. Especially considering the typically high cost of novel nanostructured catalysts, it is important that the material expense can be amortised across a significant period of operation.

Researchers strive to report promising results across all these figures of merit. This is discussed with examples in the literature review.

Chapter 2

2. Literature Review

According to the objectives laid out in the previous chapter, significant advancements have been made in recent years for CO_2 conversion. For example, in 2020, a current density of 1 A/cm^2 was first reported [7], a figure which indicates the scale of capital investment required for eventual commercialization. While this figure was a marked improvement compared to previous works, current density alone is not enough to solve this challenging problem. The second metric is product selectivity. State-of-the-art systems can put as much as 95% of the input electrons into carbon monoxide, while the best ethanol electrolyzer exhibits only 68% current efficiency [8]. A third key performance metric is stability, not only of the catalyst material, but of the entire cell, which includes another electrode, a membrane, and importantly water and salt, which must be managed. Reactor cells and their contained catalysts should be stable for thousands of hours [8]. Notwithstanding recent achievements, there is still significant work to be done in the field of electrochemical CO_2 conversion.

2.1. Strategies for Carbon-Carbon Coupling

As the title implies, the focus of this thesis is the conversion of CO_2 into multicarbon (C_{2+}) products. In the following subsections, various strategies to drive selectivity towards multicarbon products will be described. While all system components can drive performance along the figures of merit, the focus will remain on the catalyst materials themselves. Significant work has been done to map out the possible reaction pathways and variables they depend on [9], this section will focus on the catalyst features relevant to the step of C-C coupling.

To produce multicarbon products, rather than desorbing electrochemically reduced C_1 species such as CO, it is necessary that nearby C_1 intermediates be stabilized on the catalyst to bond with one another. Named carbon-carbon coupling, this critical reaction step in the production of multicarbon products is a major point of focus for rational catalyst design [10]. Copper is the best pure metal for electrocatalytic conversion to multicarbon products, and therefore provides the starting point for many researchers seeking to reach new levels of performance.

Discussed in the following subsections are some of the strategies used to promote the production of multicarbon products. Each description is accompanied by a few high-performance examples of the implemented strategy.

2.1.1. Compound-Derived Copper

Copper-containing compounds have shown to be useful precursors for CO_2 catalysts. These materials are salts; the materials can then be processed to reduce the copper, yielding pure Cu, at least on the surface. To accomplish this, possible techniques include hydrogen reduction at high temperatures and electrochemical reduction. The latter is generally more convenient as the equipment required for this process is not more than is required for the electrochemical CO_2 reduction reaction (ECO_2RR).

During this reduction reaction process, the surface morphology of the Cu is completely reconstructed, which may introduce surface features that offer desirable active sites. While the results in this section include some examples with strong performance, there is evidence to suggest that the long-term performance of oxide-derived copper is limited [11]. That said, the stability of high-performance catalysts materials is virtually always in question; therefore, promising results obtained over shorter-term tests can still inform future catalyst design at this early stage in technological readiness.

A prominent example which implements this compound-derived strategy is a Cu catalyst made from $Cu(OH)_2$ by Zhong *et al.* [12]. To make material, the hydroxide layer was first developed on Cu foil in alkaline solution. Then, the foil was reduced electrochemically at 0.5 V vs. the reversible hydrogen electrode (RHE). The team found that the resulting surface was composed of high-index planes with low coordination; these atoms provided sites leading to efficient C-C coupling, demonstrated by a faradaic efficiency (FE) of 87% for C_{2+} products with a partial current density of 217 mA cm^{-2}.

Another example of this concept was done by Li *et al.* using CuI [13]. The researchers mixed Cu and CuI nanoparticles, and the mixture outperformed (71% FE and 591 mA cm^{-2}) both of the materials individually, suggesting some synergy between the two. The researchers recognize the surface reconstruction that occurs through the electrochemical reduction of the CuI material, however, this is not the main source of catalytic performance for multicarbon products. The group points to residual iodine species, confirmed by theoretical density functional theory (DFT) calculations, as the driver of the performance. While the report does include performance testing for 85 hours, the long-term stability of the catalyst may still be questionable as the copper may be prone to further, although slower, *in-situ* reduction.

A third example of this strategy was put forward by Chen *et al.* [14]. They synthesized Cu nanorods and performed redox cycling to create oxide-derived copper nanorods. The material yielded 83.8% C_{2+} FE at 341.5 mA cm^{-2}, another one of the best selectivity figures reported to date. Through *in-situ* observations via Raman spectroscopy, X-ray absorption spectroscopy (XAS), and isotope labelling, the group concluded

that the interfaces generated by the redox cycling of the material generated the active sites necessary for C-C coupling.

2.1.2. Interfaces

The pairing of different materials at the nanometer scale has the potential to create unique environments for effective catalysis to occur. The obvious benefit of this synthesis is the special environment of atoms at the interface of two materials, for example the interface between a substrate metal and a second metal electrodeposited on top of it, as in the first example. Going beyond this, due to the proximity of the different materials, there is an opportunity for heterogenous sites nearby one another such that the necessary intermediates are stabilized for optimal selectivity, passing from one active site to the next as the desired chemical reaction proceeds.

Wang and colleagues used this strategy in the development of a Cu@Pb core-shell structure [15]. The material was synthesized by electroreduction of the metals from a solution, resulting in a 0.7 nm Pb shell on the copper nanoparticles. In testing, the catalyst yielded 81.6% C_{2+} FE with a current density of 400 mA cm^{-2}. DFT calculations showed that the catalyst supported the formation of key intermediate species for the multicarbon products.

Another example of this interface strategy was put forward by Xiong et al. [16]. The group combined pure Cu with a AuAg alloy, giving a C_{2+} FE of 77% and a current density of 230 mA cm^{-2}. According to the report, the strong performance was the result of a tandem functioning of the materials: CO_2 is reduced into CO on the AuAg alloy, while strained and positively charged Cu sites offer an optimal environment for C-C coupling.

Sultan and colleagues presented another prominent application of the interface strategy [17]. On top of Al_2CuO_4 nanosheets, the researchers distributed CuO nanoparticles. The system achieved a current density of 600 mA cm^{-2} with a C_{2+} FE of 70.1%, significantly larger than the CuO nanoparticles alone. The combination of the materials was observed to increase adsorbed CO coverage and support C-C coupling.

2.1.3. Alloying and Doping

In a similar way that the interface of two materials can deliver a unique environment otherwise unobtainable on either material individually, the strategy of alloying and doping materials can bring tuning ability to a base catalyst material. One potential benefit over the strategy of interfaces is the density of

active sites; while interfaces generally exist only at the boundaries of grains, doping and alloying can occur throughout the material.

A high performing alloy catalyst was recently proposed by Yan *et al.* [18]. They developed ultrathin CuNi nanosheets via a ligand assembly method. After synthesizing alloys of different ratios, CuNi (equal proportions) was found to give the best performance, with a C_{2+} FE of 80.5%, and a current of 250 mA cm^{-2}. DFT calculations showed that the addition of Ni increases the binding of the CO intermediate to alloy, suggesting that the alloying plays a critical role in the C-C coupling and therefore the production of multicarbon products.

Another example implementing these concepts was reported by Peng *et al.* [19]. The team synthesized cubic copper nitride, including vacancies via an electrochemical lithiation process, obtaining Cu_3N_x. The vacancy-rich structure showed strong selectivity of 81.7% for C_{2+} products with a current of 307 mA cm^{-2}. DFT calculations validated the effect of the vacancy tuning, showing a correlation between the density of N vacancies and the energy barrier for C-C coupling.

Yan *et al.* doped Cu with F and found promising results [20]. The doped particles were formed from NH_4F and $CuCl_2$ at low temperature and verified using X-ray photoelectron spectroscopy (XPS). The doped material outperformed the control sample and yielded 70.4% FE with 400 mA cm^{-2}. Enhanced CO binding as a result of the F doping is the explanation for strong multicarbon production, supported by *in-situ* studies.

2.1.4. Metal Organic Frameworks

Metal-organic frameworks (MOFs) are an attractive strategy because of their controllable size, shape and their isolated metal atoms which can act as active sites for ECO_2RR.

Wen and coworkers presented a MOF-based catalyst implementing Cu [21]. They synthesized a catalyst comprising a Cu-S motif distributed throughout the MOF HKUST-1, which delivered 88.4% C_{2+} FE with a current of 400 mA cm^{-2}. The researchers proposed that they could replicate the slight positive charge on Cu that exists in high performance oxide-derived catalysts, without the stability issues. DFT calculations support the performance of the catalysts for C-C coupling.

Implementing MOFs to obtain multicarbon products was also done by Wang *et al.* [22]. They created MOFs that used Cu as active sites with geometry tuned by the selection of another MOF component element. This component atom changed the distance between two Cu sites on the MOF, and thus this

could be optimized for C-C coupling. The MOF using hydrogen had the best C_{2+} FE, at 60%, with a current of 346 mA cm^{-2}.

While not technically a MOF, implementations of N-doped C with Cu have proven promising for ECO_2RR to multicarbon products; Wang and coworkers presented a strong recent example [23]. To prepare the electrode, the team sputtered a layer of N-doped C on top of sputtered Cu. The catalyst showed 93% C_{2+} FE at 300 mA cm^{-2}. The N-doped C was reported to promote C-C coupling via its ability to donate electrons.

2.2. Catalyst Features Relevant to the Works in this Thesis

2.2.1. Single Atom Catalysts

Single atom catalysts are a class of materials which offer promise for various future energy applications, including CO_2 conversion. They consist of a support material and an atomically dispersed element serving as an active site. When the atoms are optimally distributed on the support material surface, each atom can act as an individually useful catalytic site, which can be economically important for high-cost elements such as the noble metals.

This advantageous efficiency in material usage is quantified with specific activity, the catalytic production rate per unit mass of the single atom element. Another advantage of single atom catalysts is their uniformity in sites. Because all the active sites are single atoms, the variability in the local environment is limited. This homogeneity of sites theoretically limits side reactions as the optimally designed single atom sites will catalyse only the desired reactions, thereby increasing selectivity.

Another advantage of single atom catalysts is the ability to combine the single atom sites with additional active sites, leveraging the tandem catalyst concept proven in literature [24]. The single atom sites can be used to catalyse some reaction steps, while a different material, perhaps another material mounted on the support, or the support material itself can be used to catalyse other reaction steps.

The synthesis of single atom catalysts generally uses wet chemistry techniques to distribute the atoms on support material. The synthesis of single atom catalysts used in this thesis is described in the methods section. The characterization of single atom catalysts includes various techniques. One demonstrative test is atomic-resolution high-angle angular dark-field scanning transmission electron microscopy (HAADF-STEM), where the single atoms of a different element can be identified by their Z contrast.

2.2.2. High-Entropy Alloys

High-entropy alloys (HEAs) are a class of alloys which contain multiple elements in significant concentrations, typically five or more metals with concentrations of 5-35 at.% [25]. The origin of the name, high-entropy alloy, for this class of materials comes from Yen *et al.* who reasoned the feasibility of forming such a metallic solution, rather than the formation of intermetallic compounds [26]. They theorized that, when the number of elements is increased, the total free energy would be lower as a mixed, solid solution

than if it were formed into intermetallic compounds. As with any novel alloy, the mechanical properties and catalytic potential are unique.

Beyond simply being a new material, there are a few specific features of interest for catalysis present in HEAs [27]. First, we have what is called the cocktail effect, which arises from the solid solution of metals. Because the of the mixing of elements at the atomic level, the electronic character each atom, which is affected by the other atoms surrounding it, is the result of various factors, including the element and geometry of coordinating atoms. This results in a material that can be more than the sum of its parts.

Another effect is the lattice distortion seen in HEAs. Because the metals have a variety of sizes and bond energies with their neighbouring atoms, a significant lattice strain arises. This strain induces a large population of activated electrons, facilitating electron transfer [28], an integral part of the electrochemical reduction of CO_2. This can promote reaction pathways requiring numerous electron transfer steps and accelerate the rate of reaction.

A third effect showing the potential of HEAs for catalytic applications is the sluggish diffusion effect. By their nature, HEAs prevent migration of atoms throughout the lattice, which is understood to be a result of the heterogeneity of the lattice potential energy [27]. This effect is important for the long term stability of a catalyst; pure metals, by contrast, can undergo restructuring during the reaction, leading to reduced catalytic performance.

One of the clear challenges in study HEAs is in the computational modelling. Creating a model will require assumptions about the distribution of the atoms around the active site, whose elemental identity might also be unknown. In practice, it is likely many possible configurations of atoms will need to be considered until finding one that aligns with the performance. This modelling would be aided greatly by comprehensive characterization and in-situ study, which will help avoid unnecessary assumptions.

Chapter 3

3. Methods

Here are described the synthesis techniques used to prepare catalyst materials in the experimental works in this thesis. Specifics are given in the relevant experimental chapters.

3.1. Synthesis Techniques

3.1.1. Galvanic replacement

The first experimental work, presented in Chapter 5, utilizes a galvanic replacement reaction. The reaction is a single displacement reaction, of the form $A\,(s) + BC\,(aq) \rightarrow AC\,(aq) + B\,(s)$. In the work presented, atoms on the surface of solid Cu nanoparticles are displaced by Ag in the solution, leaving single atoms and, if sufficient silver is introduced, larger Ag clusters and nanoparticles. The reaction is allowed to go to completion in an ultrasonic bath. Because the reaction occurs only on the surface of the Cu nanoparticles and complete Ag coverage is not desired, the mass ratio of Cu nanoparticles, 100 nm in size, to Ag salt, is very large.

3.1.2. Electro-Shock High-Entropy Alloy Synthesis

In Chapter 6, an experimental work with HEAs is presented. The technique for synthesis of high entropy alloys generally requires the processing of the constituent metals at high temperature [27]. The method used in this work uses carbon as a substrate: activated carbon black provides a high surface area on top of carbon cloth. For the source metals, transition metal salts are chosen for their solubility in ethanol and suitable temperatures of dissociation. We then prepare an ethanol ink with equal parts of five metal salts and activated carbon black. This is airbrushed onto a strip of carbon cloth and allowed to dry in air. Next, the cloth strip is connected to a power source by its ends and a large current is passed through it in an inert atmosphere, raising the temperature. The temperature causes dissociation of the salts, whose pure metal atoms are then alloyed with the other nearby metal atoms, yielding HEA nanoparticles on the C support.

3.2. Performance Testing

3.2.1. Electrochemical Cell

The cell used for the results presented in this thesis is a three-chamber flow cell. This cell combines the research-oriented benefits of an H-cell with the performance benefits of a membrane electrode assembly. Like the H-cell, this cell allows the inclusion of a reference electrode; this electrode allows researchers to effectively study the single half-reaction at one electrode, independent of the performance of the other half reaction. Unlike the H-cell, this design incorporates a couple significant features that increase the reaction rate in the cell. The first is that the reactant flow is forced through the cell. The forced flow introduces reactants to the cell while carrying away the products. The second difference is the gas diffusion electrode (GDL), which allows gaseous CO_2 to access catalyst with little to no dissolution into the liquid, arranging a 3-phase interface comprised of a catalyst, CO_2 gas, and electrolyte solution. These effects substantially increase current density and therefore the commercial relevance of the design.

While this design is closer to commercial relevance than an H-cell, it is not the most commercially relevant cell design. That title is given to the membrane electrode assembly (MEA) cell. The primary difference between the three-chamber flow cell and an MEA is the distance between the electrodes. Positioning the electrodes closer together makes the cell more efficient, as the resistance of the electrolyte solution is effectively eliminated. This compact cell also eliminates the possibility of a reference electrode, eliminating the ability of researchers to study one half reaction in isolation. A model of the three-chamber cell is seen in **Figure 1**.

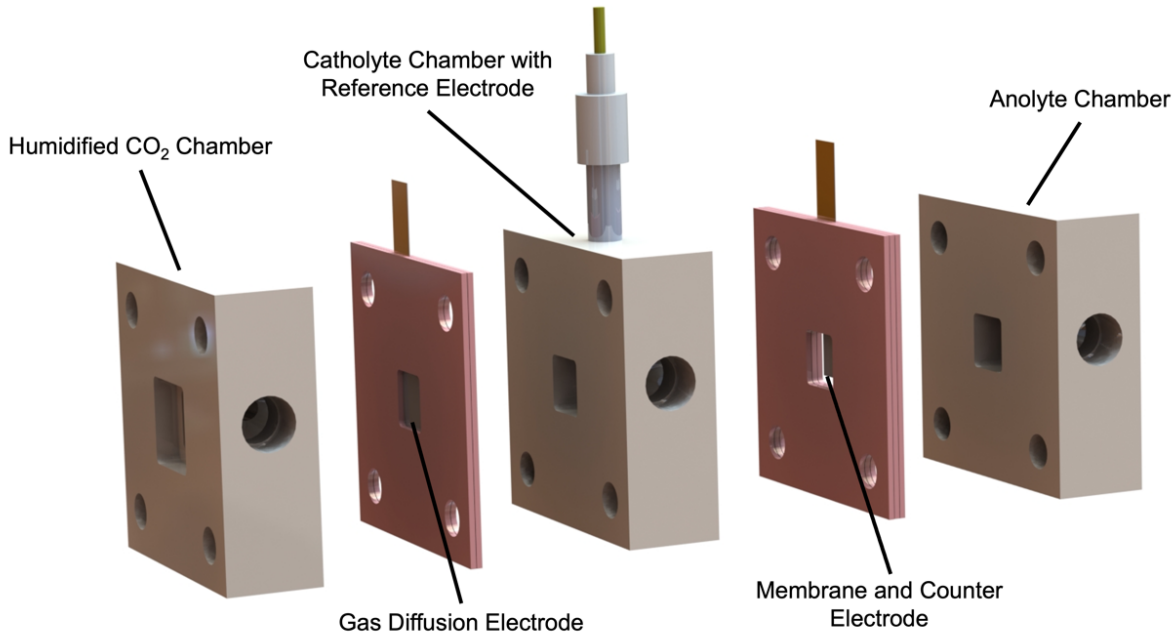


***Figure 1**. Three-chamber flow cell.*

3.2.2. Electrochemical Control and Measurement

Electrochemical testing of samples was done using a potentiostat / galvanostat, alternatively called an electrochemical workstation. The device controls the voltage or current applied to the electrochemical cell. The device used for the experimental results in this thesis is a Gamry Reference 3000. This is pictured in **Figure 2D**.

3.2.3. Quantifying Gas Products – Gas Chromatography

The device used to quantify gas products in the experimental work in this thesis is an Agilent 6890 Gas Chromatography (GC) system. It is configured with two detectors, a flame ionization detector (FID) and a thermal conductivity detector (TCD).

The FID detects analyte gases which readily combust in a hydrogen flame, with reliably consistent peaks for methane, acetylene, ethane, and ethylene at concentrations under 0.01%. To separate these gases, a CarbonPLOT 30 m x 0.320 m column was used.

The TCD is used to quantify CO, which does not manifest in the FID signal. The TCD is slightly less sensitive than the FID, which is why the FID is used when possible. To separate the gasses for this detector, a CARBOXEN 1000 column is used.

The carrier gas used in the system is helium. While this is generally the preferred carrier gas for most chromatography applications, one drawback is the lack of contrast with hydrogen on the TCD, due to their similar thermal conductivities.

In order to quantify reaction product concentrations in a sample, calibration curves were prepared. First, samples of known concentrations were injected into the GC. Then, for each analyte, the integrated peak area average of three injections was plotted over a range of concentrations and a regression analysis gave a best fit curve. These curves describe the relationship between concentration and integrated peak area. Figure S8, located in section 5.3, shows representative sample data and the standard curves.

To introduce samples into the GC, the output of the reactor cell is routed through a loop with a gas sampling valve, which, when turned, introduces a fixed volume of sample into the column. The chromatograph is pictured from the front and top in **Figure 2A-B**. In performance testing, the production rate of product of interest is determined using the concentration, as determined by the standard curve, and the reactor gas output flowrate, measured with a flowmeter (Agilent ADM flow meter).

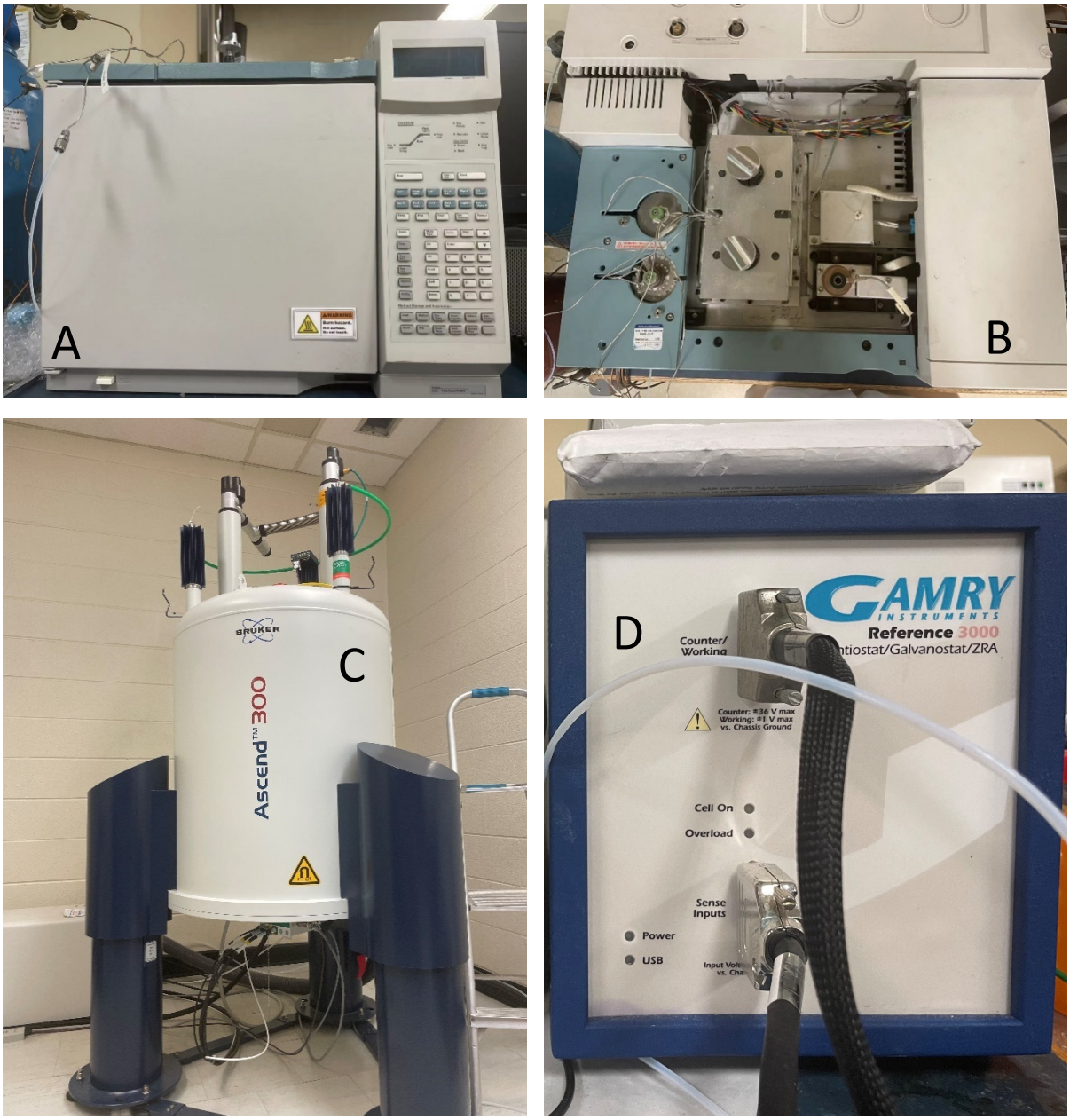


Figure 2. *Devices used for performance testing. (A) Front and (B) top views of Agilent gas chromatograph. (C) Bruker NMR spectrometer and (D) Gamry electrochemical workstation.*

3.2.4. Quantifying Liquid Products – Nuclear Magnetic Resonance Spectroscopy

In a similar way to gas product quantification, the concentration of liquid analytes is determined by proton nuclear magnetic resonance spectroscopy (NMR). Proton NMR data indicates the local environment of protons within a sample, which can be matched with known compounds. Like GC data, the magnitudes of peak areas correspond to the concentrations.

The device used for this work is the Bruker Ascend 300 MHz spectrometer, pictured in **Figure 2C**. The device, with the parameters used, can detect product concentrations on the order of 1 mM. This sensitivity enables product detection rapid testing of different reaction conditions, with meaningful results from catalyst performance tests as short as 10 minutes. One critical aspect of NMR data acquisition is the presence of water. To suppress the signal resulting from the protons in water, excitation sculpting was used. One sample was scanned 128 times (about a 10 mins).

Again, like for gas products, a standard curve was prepared with known concentrations. A range of 0mM to 8 or 10 mM, depending on the product, was tested for calibration. In addition to a fixed volume of liquid sample, D_2O and an internal standard (DMSO) were used, for locking and quantification, respectively. Figure S9 located in section 5.3 shows representative sample data and the standard curves.

3.3. Material Characterization

3.3.1. Microscopy

Electron microscopy techniques are used heavily in the characterization of catalysts for this thesis. The relatively accessible scanning electron microscope (SEM) is used for initial characterization of catalysts, offering an indication of the size and shape of nanoparticles. When paired with energy dispersive X-ray spectroscopy (EDX) capability, the device can produce elemental mapping of catalyst materials. The main limitation of the SEM for the purposes of this work is the scale; the SEM renders magnifications of up to 2 million times, while a transmission electron microscopy (TEM) system can go up to 50 million times [29]. Another difference is that SEM describes the surface of the material, while TEM renders a 2D projection of the entire volume the electrons pass through. In TEM, observing particles at an atomic scale is possible, and by using an annular dark-field (ADF) detector, elemental contrast of individual atoms is possible. Like the SEM, elemental mapping is available using EDX technology and electron energy loss spectroscopy (EELS).

3.3.2. X-Ray Diffraction

Metal catalysts generally have a crystal structure that can be described by X-ray diffraction (XRD) . In this technique, incident X-rays diffract in a direction that corresponds to the interatomic spacing of the crystal. In practice, for a signal peak to appear, the crystal must be of a certain size; therefore, very small nanoparticles are not detectable. From the data collected, the crystal phase can be deduced; in addition, the absence of a peak can indicate that a species is well distributed within a sample, provided that its presence can be confirmed by another method, as described in the next paragraph.

3.3.3. Inductively Coupled Plasma Mass Spectrometry

Inductively coupled plasma mass spectrometry (ICP-MS) uses inductively coupled plasma to ionize samples, which are then detected. The technology can detect elements at very small concentrations, in the range of milligrams to nanograms per liter [30]. The sample preparation for the analysis of metal catalysts typically requires the dissolution into solution by aqua regia.

3.3.4. X-ray Photoelectron Spectroscopy

X-ray photoelectron spectroscopy (XPS) is a technique that uses incident X-rays to induce electron emission by the photoelectric effect [31]. The emitted electrons are then seen by a detector that measures the intensity across an energy spectrum. XPS data informs the researcher of the elemental composition, as well as the electronic state of atoms in the material. As a surface-sensitive method, this characterization technique is especially relevant to catalyst study because only the first few layers of atoms are measured, a relevant depth considering the active area of catalysts.

3.3.5. Synchrotron X-Ray Absorption Spectroscopy

X-ray absorption spectroscopy (XAS) is used in this thesis to interrogate the bonds in the catalyst structure. In this system, the absorption of incident monochromatic X-rays on the sample is measured by a fluorescence detector. An experiment entails collecting the detector signal while scanning through an X-ray energy range of interest, in the case of this thesis, the metal element's K-edge. By comparing the X-ray absorption energy curve to references, we can glean information about the bonding of the element of interest.

Chapter 4

4. Technoeconomic Analysis: Evaluating the Economic Viability of Electrochemical CO_2 Conversion to Methane

4.1. Abstract

Global climate change, attributed to elevated CO_2 concentrations, has inspired significant work in carbon capture and sequestration solutions. Electrochemical CO_2 conversion promises to utilise the captured CO_2 by transforming it into useful fuels and feedstocks, minimising the need for fossil-based incumbents. In this work, we assess economic viability of electrochemical methane production from CO_2, including the cost of energy, the cost of the CO_2, and capital required to do the conversion. We arrive at a minimum cost of 11.5 cents per mole of methane, which compares unfavorably to the market price of natural gas, at 0.5 cents per mole. Alternative and new directions are discussed.

While this work focuses on methane, the major points are widely applicable to multicarbon products. This chapter provides an economic perspective for catalyst designers.

4.2. Introduction

Climate change has been strongly linked to anthropogenic increase in global CO_2 concentrations. To address this, carbon capture technologies promise to lower CO_2 concentrations. Simultaneously, fossil-based fuels and chemical feedstocks need to be replaced with alternatives if standards of living are to be maintained. One potential solution to this problem is electrochemical synthesis of these necessary commodities from CO_2.

Electrochemical CO_2 reduction was first demonstrated in the 1980s and has progressed significantly since then, with reaction rates and product selectivity rising dramatically. However, the technology has yet to be commercialized and in this work, we aim to investigate economic gap between today's systems and commercial viability.

4.3. Electrochemical CO_2 Conversion

The major components of this technology are (i) a carbon capture system (ii) an electrochemical reactor, and (iii) a product purification system. The focus of this work is the costs associated with the reactor, as this is what pertains to nanomaterial catalysts.

Inside the reactor there are two electrodes with a potential applied between them. On one, CO_2 is chemically reduced into methane. At the other, oxygen is formed and released. Between them is a water-saturated membrane, which allows the flow of ions but prevents product crossover.

The catalysts are the main area of interest for a materials scientist. Nanomaterials are implemented here for their unique properties. The large surface area of nanomaterials allows for a greater density of active sites, which offers more production from a given cell geometry. Meso-, micro-, and nano-porous structures can offer unique and preferable mass transport mechanisms, promoting the desired reactions.

Known as the Sabatier principle, the basic criterion for a heterogenous catalysts is that the interaction between catalyst and reactants be not too strong and not too weak. If too strong, reaction products will not desorb from the surface. Too weak, and reactants will not adsorb in the first place. In CO_2 conversion, the reaction pathways include many steps and different intermediate species, which makes the search for a catalyst more complex.

4.4. Determining Costs

Ultimately, the implementation of electrochemical CO_2 conversion to methane depends on the commercial viability of the process. To evaluate this, the commodity price of natural gas will be used: 6 USD per million BTU [32] (about 1 055 MJ [33]) with an enthalpy of combustion for methane of 890 kJ mol^{-1} [34], we have a price of 0.0051 USD mol^{-1}, or 0.51 US cents mol^{-1}.

The total costs of a CO_2 conversion system depend significantly on where the boundaries of the system are drawn. The most holistic analysis would begin with the costs of CO_2 capture (which could be directly from the air or from a concentrated point source) and end with the costs of getting the product to commodity market (including necessary purification and transportation steps). A holistic perspective such as this is necessary to develop the first commercially viable system as soon as possible.

To this point, there is significant evidence that the steps involved in CO_2 conversion should not be treated as discrete problems. One example of this type of approach is from Berlinguette *et. al.* who are pioneering work in bicarbonate conversion [35]; bicarbonate is a chemical intermediate in alkaline CO_2 capture systems, which simplifies the CO_2 capture process. However, it is not clear that alkaline CO_2 capture technology will be dominant, leading to the potential irrelevance of this technology. We present a second example, found at the other end of the process: Sinton *et. al* reported a technique to increase the product concentrations of liquid ethanol in the output flows by implementing a proton exchange layer in the cell [36]. Obtaining higher product concentrations is an often-overlooked target which is generally desirable as it reduces product separation (purification) costs.

Naturally, the focus of materials scientists aiming to better catalyse the CO_2 reduction reaction is on the costs of this big step in the middle, which is defined as the inputs to the electrochemical reactor cell. This is a reasonable division of the larger problem, provided that researchers give sufficient attention to the integration with state-of-the-art capture and product separation technologies. Therefore, for the purposes of this work, the conversion reactor will be treated as discrete from the capture, purification, and transfer steps.

The cost of CO_2 conversion into methane can be divided into two categories, namely operating expenses, and capital expenditures. The main operating expenses for this electrochemical reduction process are (i) electrical power, and (ii) supply of concentrated CO_2. Capital expenditures comprise reactor cells, membranes, power supplies and the all-important electrode and catalyst materials.

4.4.1. Electrical Power Input

A theoretical minimum energy input is provided by the thermodynamics of the reaction. In a complete system, there are reactions at the cathode, where CO_2 is reduced into methane, and the anode, where the oxygen evolution reaction (OER) occurs. Both reactions have a standard potential relative to the standard hydrogen electrode (SHE) that represents the minimum voltage for the half cell. We calculate the difference between these two potentials to obtain the full-cell potential. These reactions and potentials are listed in **Table 2**. This theoretical minimum potential is a starting point.

Getting as close as possible to this listed potential is one of the primary aims of catalyst research. The difference between the theoretical standard potential and the "empirical" potential required for the desired reaction to proceed at reasonable rates is called the overpotential. There is an overpotential for each half-cell, and there is a resistance to be overcome for the ions to travel through the solution between the electrodes, which is also impeded by the membrane, a needed component to prevent product crossover. Reported potentials are presented also in **Table 2**.

Table 2 *Voltages needed for the reactions to proceed, in theory and in practice*

Reaction	Standard Potential (theoretical)	Reported Results
$CO_2 + 8H^+ + 8e^- \rightleftharpoons CH_4 + 2H_2O$	–0.24 V (vs. SHE) [37]	–1.4 V (vs. RHE) [25]
$4OH^- \rightleftharpoons O_2 + 2H_2O + 4e^-$ (alkaline pH)	1.23 V (vs. SHE) [38]	1.5 V (vs. RHE) [26]
Full Cell Potential	1.47 V	

Once the required full-cell potential is known, the energy required per mole of product is straightforward. There are two considerations needed to arrive at the power consumed: (i) faradaic efficiency and (ii) the number of electrons per mole of product.

Faradaic, coulombic, or current efficiency is the fraction of the charge (or current) passing through the cell that is participating in the desired chemical reaction, namely CO_2 reduction into methane. While the figure is ideally 100%, undesired, competitive reactions inevitably take place in the cell, wasting the electrical energy. In such an aqueous system, as in these cells, the main concern is the hydrogen evolution reaction (HER). Hence, HER suppression is an area of focus in this field [39].

As indicated in **Table 2**, producing one mole of methane requires eight moles of electrons. Consider Equation 1, all S.I. units,

$$E = \frac{P * n * F}{f.e.} \qquad (1)$$

where E is the input energy, P is the full-cell voltage, n is the number of electrons required for one molecule of product, F is Faraday's constant, 96 485 C mol^{-1}, and $f.e.$ is the Faradaic efficiency. Using 100% Faradaic efficiency and the theoretical cell potential of 1.47 V, we find that the minimum energy input to convert one mole of CO_2 into one mole (16.04 g) of CH_4 is approximately 1135 kJ. Considering a more realistic 3.5 V and a faradaic efficiency of 90%, the electrical energy required increases to 3002 kJ mol^{-1}. The result of these two changes is an energy efficiency of 38%.

To obtain the cost of electrical energy to convert CO_2, we combine these more realistic energy demands with typical Ontario electricity price of 0.10 USD per kW h [40] (or 3 600 kJ), we obtain a price of 0.083 USD per mol of methane, more than 15 times the commodity price for natural gas.

It makes logical sense that such a price ratio exists: methane is a cheap and ubiquitous fuel for electricity generation via the combustion reaction, essentially the reverse of the CO_2 reduction reaction into methane. Assuming, reasonably, that the electrical energy is priced high enough to cover the cost of the fuel to generate it, we can simplify the economic argument to one of the conservation of energy: the electrical energy harvested (much less than 100% efficient) from methane combustion is not enough energy to produce the same amount of methane again via electrochemical CO_2 reduction (also much less than 100% efficient). One cannot profitably convert CO_2 to methane for commodity sale using electricity generated by the combustion of methane. Clearly, a lower-cost source of power is needed for this conversion. It also follows that methane is not a target product.

Turning to renewables and looking forward, the U.S. Department of Energy anticipates a drop in the cost of solar energy to 0.03 USD per kW h by 2030 [41], a fraction of Ontario's current price. This 70% drop will be a welcome change, bringing the cost down to 0.025 USD mol^{-1}, which is 4.9 times the current commodity price. Running the reactors at off-peak times and getting preferred pricing by strategically locating the conversion facilities near power sources will bring the electricity costs down further.

Bottom line – energy costs: 0.025 to 0.083+ USD per mole CH_4 produced.

4.4.2. Cost of Carbon Dioxide

Importantly, the use of low-purity CO_2 sources, such as flue gas (18-20% CO_2) [42] or the atmosphere (300 ppm), gives way to the prohibitively competitive oxygen reduction reaction (ORR) [43]. Therefore, it is

vital to consider the costs of obtaining high-purity CO_2 in a technoeconomic analysis of the system. Current CO_2 capture technologies are reported to have fallen below 100 USD per ton [44], which amounts to 0.0044 USD per mole of CO_2. Clearly, there is a need for a lowering of costs in this area.

What makes this challenge worse is that many electrochemical conversion systems convert only a fraction of the CO_2 introduced into the cell. Theoretical limits on the carbon efficiency, which vary with the product produced and the pH in the cell [45], place methane well under 50% carbon efficiency in a typical configuration. Realistic conditions, where much of the CO_2 flows through the cell and never touches the catalyst, make this figure worse. Some recent reports show that high carbon efficiency of 85% is possible [46]; this often-ignored metric should be reported and optimised more often.

There is some good news on this front. Carbon tax programs, where in California for example, the price of carbon is 65 USD per ton [47], would reduce the cost of CO_2 significantly. Assuming further advancements in carbon capture, the price could be zero or even negative.

Bottom line – CO_2 costs: 0 to 0.0044+ USD per mole CH_4 produced.

4.4.3. Capital Expenditures

Capital expenditures include the investment in electrolysers, pumps, and electrical equipment. To obtain a sense of these costs, an amortization period and current density must be assumed. A benchmark for a CO_2 conversion system is 200 mA cm^{-2} [8], which translates to 8.2 mol yr^{-1} cm^{-2} of product. At a price of 31 USD cm^{-2} for currently available research-grade hardware [48], an amortization period of 30 years gives a cost per mole of 0.09 USD mol^{-1} of CH_4 produced.

While equipment costs could be expected to drop significantly with mass-manufacturing, this figure is likely an appropriate baseline given that the catalysts (with lifetimes likely much less than 30 years), pumps, and electrical equipment are not yet taken into consideration. Developments on the current density would be most welcome, as this will reduce electrolyser costs.

Other estimates of the cost of this equipment are considerably lower. Reference values for the electrolyser stack cost in highly-cited papers on this topic are 230 USD kW^{-1} [5], compared to approximately 4.4 kUSD kW^{-1} estimated here. Notably, this optimistic report uses the bulk metal market price of Cu and Ir for catalyst costs and allocates just a few mg cm^{-2} loading on the electrodes, apparently ignoring the cost of material processing and electrode preparation.

Bottom line – Capital costs: 0.09 USD per mole CH_4 produced.

4.5. Conclusions

When the costs from these three studied components are combined, it becomes clear that it will be difficult for electrochemically produced methane to displace natural gas. The current commodity price of 0.51 cents per mole is much less than the estimated minimum cost of 11.5 cents per mole for electrochemically produced methane, calculated here. It makes some sense, when we consider that natural gas is one of the most cost-effective fuels for electricity production [49], that that essentially reversing the combustion reaction, using electricity, is not going to be profitable.

While not compared explicitly here, the economics of methane production are less favorable than other potential products. An example is methanol, which has an oxidation state requiring three quarters (6 vs. 8) of the electrons needed for methane, and a commodity market price of 400 USD per metric ton [50], or about 0.013 USD per mole (vs. ~0.005 for methane). Formic acid and C_2 products hold even more promise of profitability [3].

One avenue for this technology is to postpone the commoditization of the output in favour of producing a differentiated, “green” product that consumers are willing to pay a premium for. An example of this strategy is that of Ocean Cleanup, an organization that recycled plastic they recovered from the ocean into a pair of 199 USD sunglasses [51], forgoing the recycled plastic commodity market.

We, the authorship, do not recommend further work on the production of methane from CO_2 via electrochemical means. There are investments to be made with much better opportunity for returns. Within electrochemistry, there are other CO_2 reduction products, particularly those with higher commodity prices. Outside this field, energy conservation, low-cost, clean energy, and production systems for carbon capture and sequestration are also needed.

The future will likely hold a variety of clean technologies that meet our energy needs while managing greenhouse gasses. Carbon capture, conversion and sequestration are all very energy intensive processes, and so accessing energy cheaply is important to achieving the vital goal of reducing global CO_2 concentrations. It is hoped that this technoeconomic analysis provides an example to evaluate future solutions to this global problem and gives material scientists an economic perspective when designing catalysts.

Chapter 5

5. Achieving 94% Faradic efficiency toward multicarbon products in CO_2 electroreduction via synergy between AgCu single-atom alloy and Ag nanoparticles

5.1. Abstract

Electrocatalytic CO_2 reduction into value-added multicarbon products offers a means to close the anthropogenic carbon cycle using renewable electricity. However, the unsatisfactory catalytic selectivity for multicarbon products severely hampers the practical application of this technology. In this work, we develop a novel cascade AgCu single-atom and nanoparticle (SANP) catalyst, in which an Ag nanoparticle (NP) produces CO and an AgCu single-atom alloy (SAA) promotes C-C coupling kinetics. As a result, a record high Faradaic efficiency (FE) of 94% toward multicarbon products was achieved over the as-prepared AgCu SANP, under ~720 mA cm^{-2} working current density in a flow cell. Density functional theory (DFT) calculations further demonstrated that the high multicarbon product selectivity is a result of synergy between AgCu SAA and Ag NP.

5.2. Main

Electrocatalytic CO_2 reduction into valuable chemicals utilizing renewable electricity provides a sustainable route for CO_2 recycling and utilization, playing a critical role in realizing a carbon-neutral cycle.[3, 52] In the past decades, enormous progress has been achieved for single-carbon product generation in electrocatalytic CO_2 reduction reaction (CO_2RR), especially for carbon monoxide and formic acid.[53, 54] However, the low value of C_1 products severely limits the application of electrocatalytic CO_2RR technology.[55-57] Thus, producing multicarbon products from CO_2RR seems much more attractive.[58] Since Hori et al. firstly reported the production of multicarbon products (C_2H_4, C_2H_5OH, CH_3COOH, n-C_3H_7OH, etc.) on copper (Cu) in 1989, Cu has been demonstrated to be the only metal that can effectively catalyze CO_2 into multicarbon products.[59, 60] The sluggish C-C coupling kinetics over pure Cu surface severely hinders industrial-level production of multicarbon products.[61-63] Therefore, various catalyst design strategies have been developed to improve the multicarbon product performance of Cu-based catalysts, for instance, alloying, doping, surface modification, interface engineering, etc.[64-67]

Inspired by the complex multistep cascade reactions in enzymes, Peter et al. put forward a cascade catalysis strategy to improve the multicarbon production with an Ag@Cu core-shell structure catalyst.[68] The CO_2 can be reduced into CO on the Ag core and then transferred to the Cu shell for further reduction into multicarbon products.[68] Based on a similar tandem catalysis mechanism, Chen et al. improved the C_{2+} partial current over Cu catalyst from 37 to 160 mA cm^{-2} by simply adding Ag nanoparticles to the catalyst, proving the effectiveness of cascade catalysis under industrial current densities.[69] Very recently, Zhang et al. applied such a cascade catalysis mechanism to gas diffusion electrode (GDE) design.[70] To be specific, they prepared segmented tandem electrodes in which a CO-selective catalyst layer (CL) segment at the inlet prolongs CO residence time in the subsequent C_{2+} selective segment, resulting in 90% C_{2+} FE over Cu/Fe-N-C catalysts. These examples strongly confirm the practicability for C_{2+} production of such a cascade CO_2RR mechanism, which integrates two consecutive steps of CO_2-to-CO and CO-to-C_{2+} on two distinct catalytic sites. However, the C-C kinetics are usually dominated by two factors: surface coverage of local adsorbed carbon monoxide (*CO) and adsorption energy of *CO.[62, 70, 71] Almost all of the reported catalyst designs in cascade CO_2RR systems have focused on improving the surface coverage of adsorbed *CO by enhancing local CO concentration, ignoring the adsorption energy of *CO on the Cu surface.

Based on such understanding, in this work, we develop a novel cascade catalyst in which an AgCu single-atom alloy (SAA) serves as a C-C coupling site while Ag nanoparticles (NP) produce CO locally. In particular, the Ag single-atom doping of Cu NP can greatly improve the adsorption energy of *CO on Cu sites due to the asymmetric bonding of the Cu atom to the enamouring Ag atom, resulting in a much better C-C coupling ability than that of pure Cu NP. As a result, the as-prepared AgCu single-atom alloy and Ag NP (denoted as AgCu SANP) catalysts exhibited 94% FE toward multicarbon products under ~720 mA cm^{-2} working current density in a flow cell, which set a landmark for multicarbon products' selectivity in electrocatalytic CO_2RR. Our DFT calculations indicate the high C_{2+} selectivity mainly originates from the preferred reaction pathway on AgCu SAA.

5.2.1. Characterization of Catalysts

The AgCu catalysts were prepared through the galvanic replacement reaction between commercial Cu NPs and Ag^+, which was spontaneously driven by their reduction potential difference. As schemed in **Figure 3A**, the dispersion of Ag atoms varies with increasing the amount of Ag^+. As a result, AgCu SAA, AgCu SANP, and AgCu NP were synthesized by simply tuning the amount of Ag^+. The scanning electron microscope (SEM) images (**Figure S1**) show that all AgCu catalysts present similar morphology of aggregation with a size between 100 nm to 200 nm. The bright-field scanning transmission electron microscopy (BF-STEM) images (**Figure 3B** and **Figure S2A**-B) further prove the aggregation morphology. From the high-angle annular dark-field scanning transmission electron microscopy (HAADF-STEM) images (**Figure 3C** and **Figure** S2C-F), some small Ag NP can be found in AgCu SANP due to the Z contrast difference between Ag and Cu. Further aberration-corrected HAADF-STEM (AC-HAADF-STEM) images (**Figure 3D**, **Figure** S3D) show many bright dots in the Cu crystal lattice, which are ascribed to Ag single-atoms. The HAADF-STEM images and energy-dispersive X-ray spectroscopy (EDS) element mapping demonstrate the existence of separated Ag NP and uniform dispersion of Ag and Cu elements in other parts of AgCu SANP (**Figure 3E**). These results confirm the co-existence of Ag NP and Ag single-atom in the AgCu SANP. As a comparison, the Ag atoms are uniformly and atomically dispersed in the AgCu SAA (**Figure S3E**).

To further study the structure and composition of AgCu SANP, grazing incidence X-ray diffraction (GI-XRD) was measured (**Figure 4A and Figure S4)**. The intensity of Cu (111) and CuO (002) and (111) peaks gradually decrease with the increase of Ag in the samples, accompanying the increase of Ag (111) and (200) and Cu_2O (111) and (200) peak intensity. In detail, AgCu SAA shows a similar XRD spectrum to Cu NP, indicating the high atomic dispersion of Ag atoms in AgCu SAA. There are both Ag and Cu peaks in

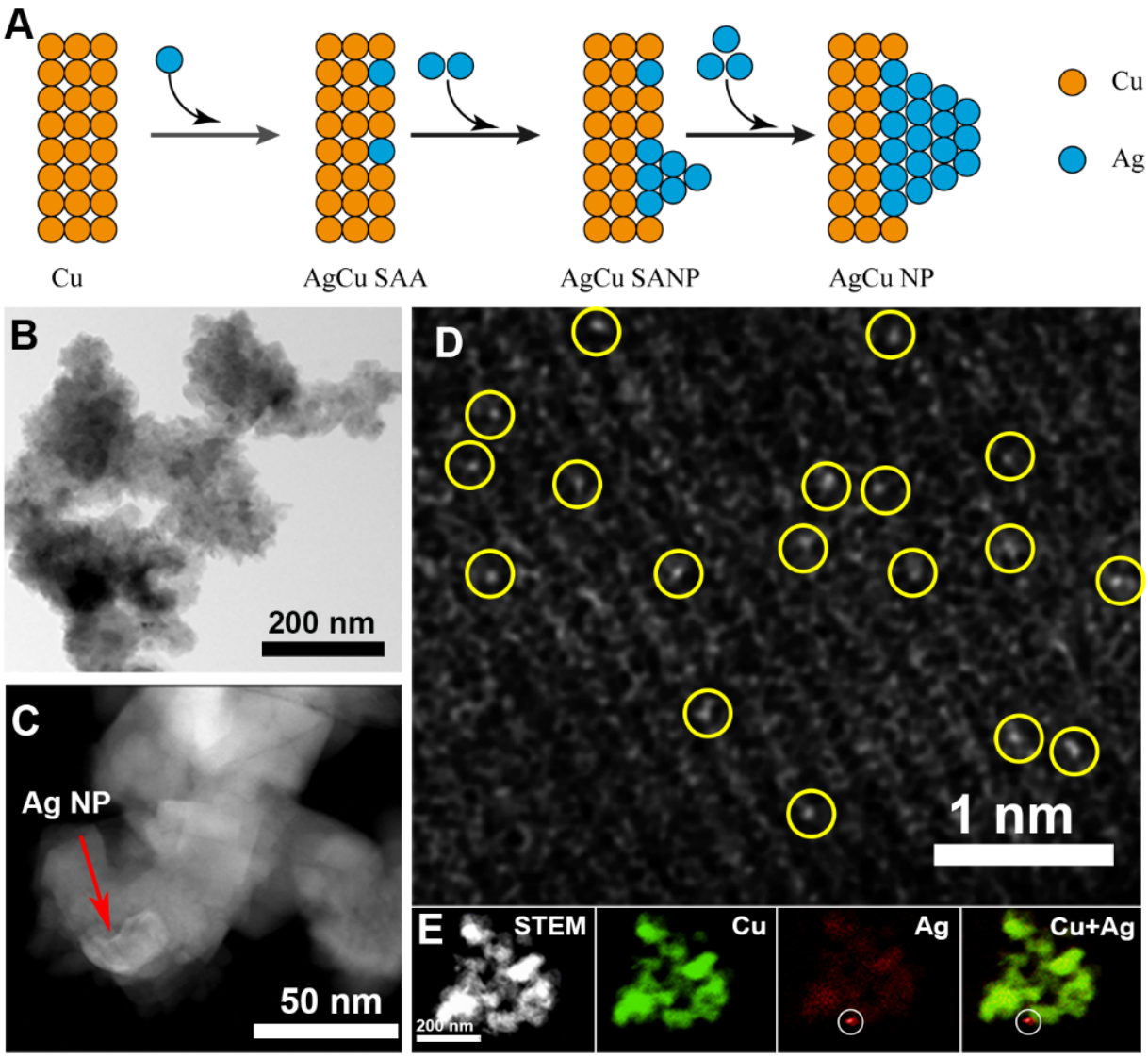


Figure 3. *Scanning transmission electron microscopy imaging of catalysts. (A) Scheme of the synthesis process of AgCu catalysts; (B) BF-STEM image of AgCu SANP; (C) HAADF-STEM image of AgCu SANP; (D) AC-HAADF-STEM image of AgCu SANP; (E) STEM and EDS element mapping images of AgCu SANP.*

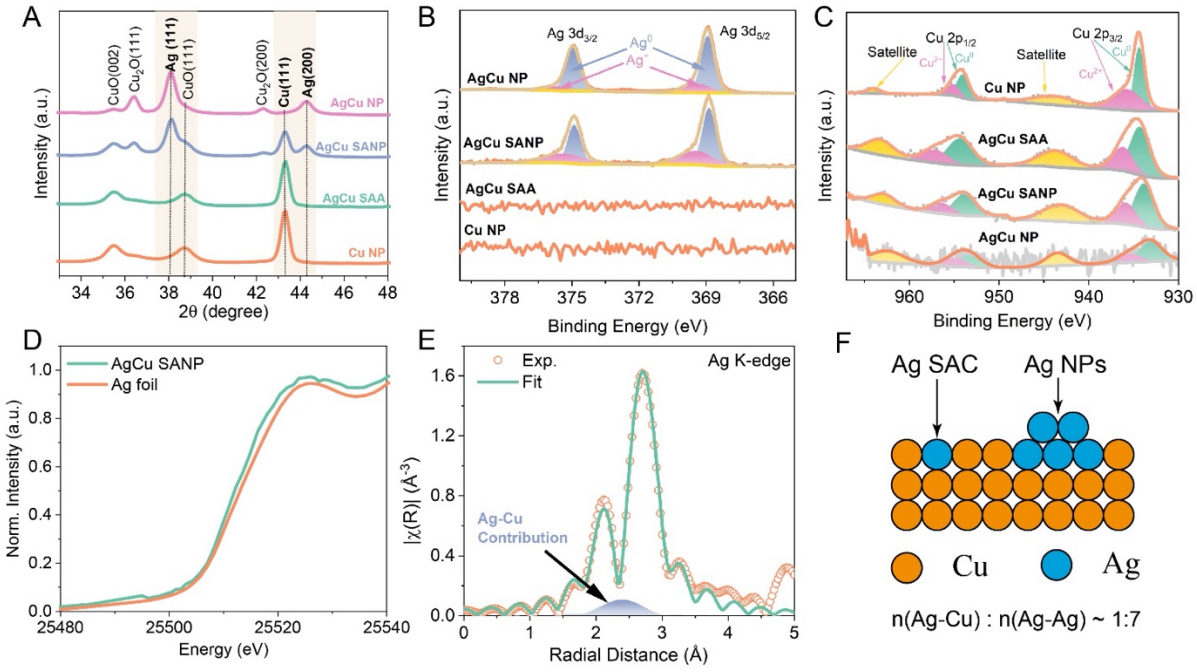


Figure 4. *X-ray diffraction and spectroscopies characterization of catalysts. (A) XRD spectra, (B) Ag 3d core-level XPS spectra, (C) Cu 2p core-level XPS spectra of Cu NP, AgCu SAA, AgCu SANP, and AgCu NP; (D) Ag K-edge XANES spectra of AgCu SANP and Ag foil; (E) Ag K-edge XAFS experimental and fitting spectrum of AgCu SANP; (F) Scheme of AgCu SANP structure and the ratio of Ag-Cu and Ag-Ag contribution from fitting results.*

AgCu SANP, confirming the existence of Ag NP and agreeing well with the STEM results. One should note that it contains Cu (111), (200), and (220) reflections in all the samples (**Figure** S4), which indicates Cu is polycrystalline. X-ray photoelectron spectroscopy (XPS) was further tested to study the elemental valence. Only AgCu SANP and AgCu NP show apparent Ag peaks, which can be deconvoluted into the four peaks of $3d_{3/2}$, $3d_{5/2}$ of metallic Ag, and Ag oxide (as marked in **Figure 4B**). The disappearance of the Ag XPS peak in AgCu SAA may be caused by the low content of Ag, which is 0.04 ωt.% determined by inductively coupled plasma mass spectrometry (ICP-MS). The core-level Cu 2p XPS peak can be deconvoluted into six peaks, corresponding to $2p_{3/2}$, $2p_{1/2}$ of Cu^0, Cu^{2+}, and shake-up peaks (as marked in **Figure 4C**).[72, 73] In addition, the intensity of Ag and Cu XPS peaks also exhibit a similar trend to that of XRD spectra, in which Ag increases and Cu decreases with the increasing amount of Ag in the samples. This also agrees well with the galvanic replacement reaction mechanism. ICP-MS results show that the detailed content of Ag in AgCu SAA, AgCu SANP, and AgCu NP increased from 0.04 ωt%, 1 ωt% to 4 ωt%.

The coordination structure of Ag species in as-synthesized AgCu SANP was further investigated by synchrotron-radiation-based X-ray absorption fine structure (XAFS) at the Advanced Photon Source (APS), Argonne National Laboratory. As shown in the Ag K-edge X-ray absorption near-edge structure (XANES) spectral (**Figure 4D)**, the adsorption edge (E_0) around 0.5 of AgCu SANP shows a slight shift to lower energy compared to that of Ag foil, indicating electron transfer from Cu to Ag due to the formation of Ag-Cu bond. The positive shift of the adsorption edge of AgCu SANP in the Cu K-edge also demonstrates the electron loss of Cu (**Figure S5**). Moreover, the Fourier transform (FT) of the k^2-weighted extended X-ray absorption fine structure (EXAFS) curve of the Ag K-edge of AgCu SANP shows both Ag-Ag and Ag-Cu coordination bond (**Figure 4E**). As schemed in **Figure 4F**, the ratio of Ag-Cu bonds to Ag-Ag bonds was estimated to be around 1:7 based on the extended X-ray absorption fine structure (EXAFS) fitting results (**Figure S6** and **Table S1**). These results strongly indicate the co-existing of single-atom and NP Ag in AgCu. Combining the XANES, EXAFS analysis and AC-STEM images, the co-existence of Ag and Cu atoms in the AgCu SAA has been confirmed.

5.2.2. Performance of CO_2 reduction and CO reduction on the catalyst

To demonstrate the cascade catalysis concept on the C_{2+} production (**Figure 5A**), the electrocatalytic CO_2RR performance of AgCu SANP and other controlled samples were tested in a flow cell with 1M KOH as an electrolyte, as shown in **Figure S7**. Specifically, potentiostatic testing was conducted on AgCu catalysts under different potentials. The gas products were collected and quantified by in-line gas

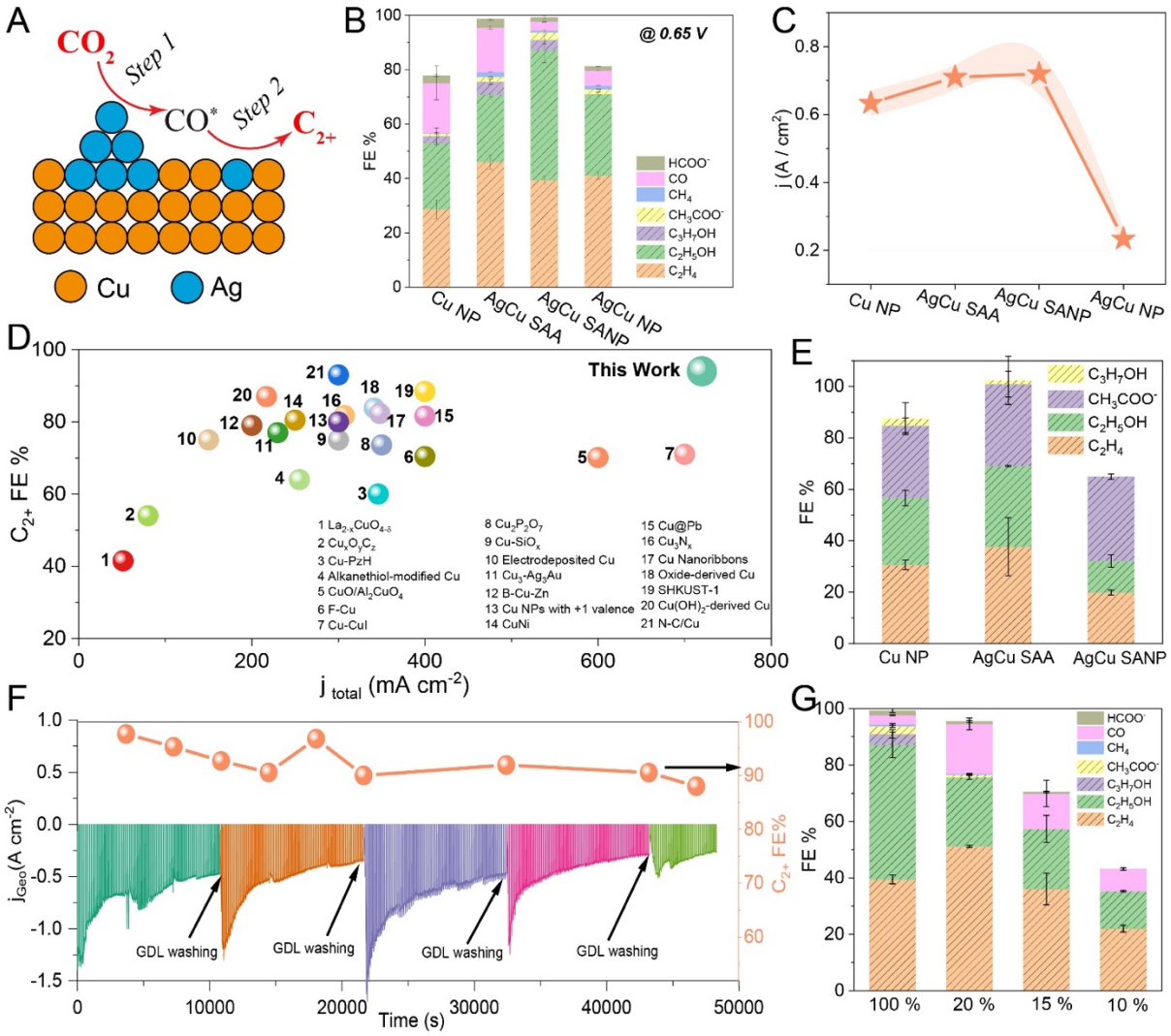


Figure 5. *Electrocatalytic CO_2 reduction and CO reduction performance of the catalysts. (A) Scheme of the cascade catalysis mechanism over AgCu SANP; (B) FE results of Cu NP, AgCu SAA, AgCu SANP, and Ag NP catalysts toward CO_2RR at -0.65V; (C) Total current density of Cu NP, AgCu SAA, AgCu SANP, and Ag NP catalysts at -0.65V; (D) Performance comparison of AgCu SANP and reported results; (E) FE results of Cu NP, AgCu SAA and AgCu SANP toward CO reduction; (F) Long-term stability results of AgCu SANP toward CO_2RR; (G) FE results of AgCu SANP toward CO_2RR feeding with different CO_2 concentrations.*

chromatography (**Figure S8**), while the liquid products were directly dissolved in the electrolyte and analyzed by nuclear magnetic resonance (NMR) (**Figure S9**). The C_{2+} products are mainly ethylene and ethanol with minor acetate and n-propanol for all catalysts (**Figure 5B, Figure S10**). Typically, AgCu SANP exhibits an ultrahigh C_{2+} FE of 94% under -0.65V, which is much higher than that of Cu NP (56%), AgCu SAA (78%), and AgCu NP (73%) (**Figure 5B**). The apparent current density under -0.65 V of AgCu SANP (720 mA cm^{-2}) is also larger than that of Cu NP (630 mA cm^{-2}), AgCu SAA (710 mA cm^{-2}) and AgCu NP (233 mA cm^{-2}) (**Figure 5C**). In addition, the C_{2+} production performance of as-prepared AgCu SANP is also superior to most of the reported catalysts (**Figure 5D**). This activity performance strongly confirms the superiority of AgCu SANP in C_{2+} production, indicating the success of the proposed cascade catalysis concept. It is worthwhile to note that all the copper oxides in the as-synthesized catalyst were reduced to the metallic state during the negative potential.[74] The FE of CO production is the least in AgCu SANP, which indicates most of the CO was converted to C_{2+} products via C-C coupling. As mentioned before, the concept of this proposed AgCu SANP cascade catalysis is that the Ag single-atom on Cu can promote the C-C coupling kinetics, while the Ag nanoparticles can produce local CO from CO_2. To further prove this point, CO reduction experiments were carried out to study the C-C coupling kinetics. As presented in **Figure 5E**, AgCu SAA presents a much higher FE than that of Cu NP, strongly indicating the improvement of C-C coupling kinetics by Ag single-atom in Cu lattice. The low FE of AgCu SANP for CO reduction can be ascribed to Ag NP composition, which excludes the adsorption of CO and hampers further CO reduction. This easy desorption of CO from Ag sites is also confirmed by the density functional theory (DFT) calculation (**Table S3** and **Figure S14**). It is worthy to note that the FE of ethanol and ethylene (green plus orange region) in CO_2 reduction (**Figure 5B**) and CO reduction (**Figure 5E**) were comparable on AgCu SAA and Cu NP. In comparison, the FE of ethanol and ethylene (green plus orange region) in CO reduction on AgCu SANP significant decrease from 87.1% (**Figure 5B**) to 32.2% (**Figure 5E**). This is due to the easy desorption of CO from the Ag NP, which decreases the local concentration of CO on the catalyst surface. This also confirms the existence of Ag NP in AgCu SANP and the cascade catalysis mechanism of AgCu SANP for CO_2RR. The FE of acetate formation is similar for CuNP, AgCu SANP, and AgCu SAA in CO reduction (**Figure 5E**). This indicates the formation of acetate is on the Cu active sites which are independent of Ag content. To alleviate the flooding issue in the flow cell, long-term stability was tested using a pulse electrolysis method (working 90s and off 30s) with a polytetrafluoroethylene (PTFE)-based gas diffusion electrode (GDE) according to a previous report.[75] Although the current density decreased due to the flooding problem, the C_{2+} FE only decreases a little from 98% to 88% during the 13h test (total working time 9.75h) (**Figure 5F**).

To show the potential of as-prepared AgCu SANP in practical CO_2 reduction applications in the industry from flue gas, its catalytic activity with a diluted CO_2 gas feed was also studied. As shown in **Figure 5G** and **Figure S11**, AgCu SANP still keeps very high CO_2RR activity when the concertation of CO_2 feeding gas decreased to 20%, exhibiting 95% FE toward CO_2 reduction with 76% C_{2+} production FE. With decreasing CO_2 gas concentration, the C_{2+} FE decreased to 57% (70% for total CO_2RR) and 35% (43% for total CO_2RR) with 15% and 10% CO_2 gas concentrations, respectively. This performance strongly indicates the promising application of AgCu SANP in practical conditions. Therefore, CO_2 enrichment processes are needed to maximize the catalytic performance in converting flue gas.

5.2.3. Mechanistic study using density functional theory calculations

Our experimental study reveals that ethanol and ethylene are the most common C_2 products on the AgCu SAA catalyst with a slight amount of acetic acid. Both ethanol and ethylene require 12 coupled electron protons, while the formation of acetic acid involves 8 coupled electron protons [76-78]. To model AgCu SAA, we adapt an Ag-doped Cu model structure. To get insight into the atomic scale CO_2 reduction reaction mechanism toward ethylene, ethanol, and acetic acid on the Ag-doped Cu catalyst surface, we performed a detailed mechanistic study considering the possibility of forming different intermediates using DFT calculations. The Cu was confirmed to be polycrystalline in the experiment (**Figure** S4). However, for our simulation, we model the (100) facet of Cu because it favors C_2 products over the C_1 products as recommended in the previous literature [79]. The CO_2RR to C_{2+} products involve various intermediates with the C-C coupling being the rate-determining step [80]. The possible intermediates in each elementary step across the reaction coordinate were examined in **Figure S12.** The minimum energy pathways are shown in **Figure 6**. Prior studies have reported that on Cu electrodes, the C-C coupling can occur through *CO-*CO dimerization, *CO-*CHO, or *CO-*COH with *CO-*CO coupling being less feasible with a higher transition state (TS) energy (> 1 eV) [81-83]. The barriers for hydrogenation of *CO to *CHO and *COH on Cu(100) are 0.64 and 0.94 eV respectively, which are more favored than the direct CO-CO coupling (> 1 eV) [84]. Thus, we choose to investigate the less energetic C-C coupling barriers, i.e., *CO-*CHO and *CO-*COH on the Ag-doped Cu(100) surface. The Ag doping creates a surface strain because of its larger atomic radius. In pure Cu(100) surface the Cu-Cu bond length is 2.57 Å, however, after doping, this is compressed to 2.50 Å at the surface. The compressive strain creates asymmetrical sites next to the Ag atom (i.e., first-neighbor atoms labeled 'B', **Figure S13)**, which provide active sites for the C-C coupling. As shown in **Figure 6A**, the TS values of C-C coupling via *CO-*CHO and *CO-*COH reactions are 0.51 and 1.10 eV, respectively, which agree well with the

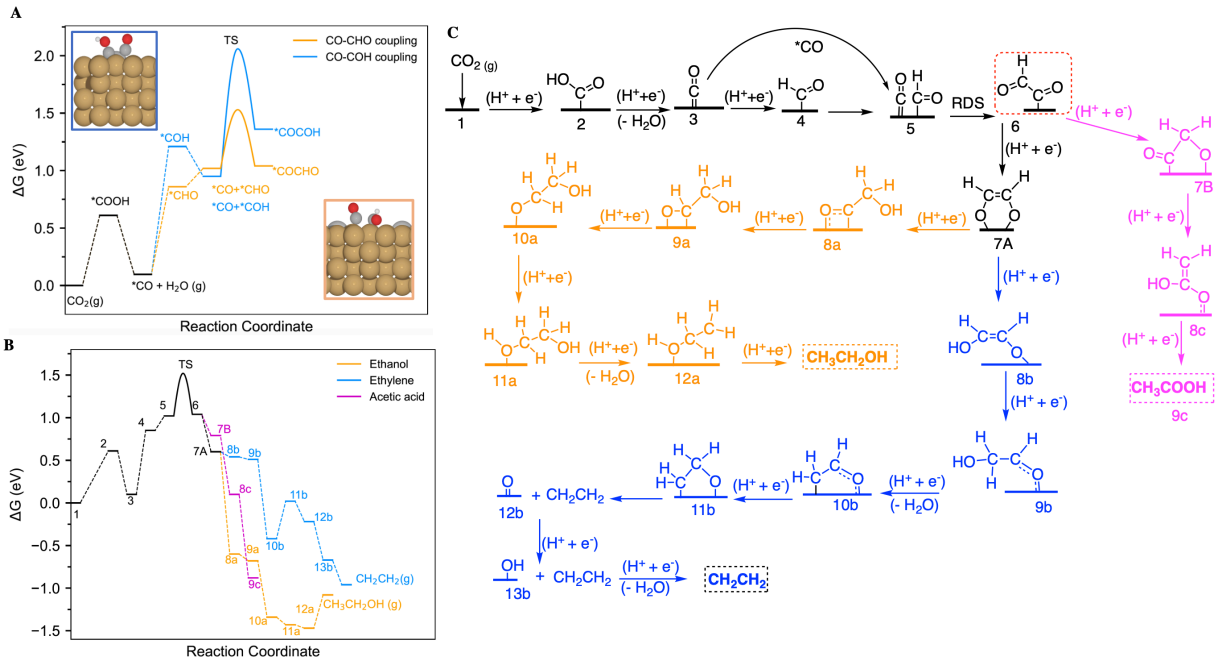


Figure 6. *Mechanistic studies by the density functional theory calculations. (A) Comparison of the C-C coupling activation barrier for the *CHO and *COH intermediates; (B) the lowest free energy pathway for the formation of ethanol (orange), ethylene (blue), and acetic acid (magenta), and (C) the associated chemical formula for each elementary step. Courtesy of Professor Samira Siahrostami, Dr. Asfaw Yohannes, Dr. Jian Xiang Lian at the University of Calgary.*

previously reported numbers on Cu(100) [81]. To understand the effect of Ag on the reactions, we also calculated the TS barrier of *CO-*CHO on the pure Cu(100) surface. A transition state energy of 0.55 eV barrier is obtained, which is slightly higher than the Ag-doped Cu(100) surface. The main difference between the selectivity of Cu(100) and Ag-doped Cu(100) thus comes from the fact that Ag is deemed to produce CO from CO_2. [85] CO is not stable on the Ag atom and easily diffuses to the next Cu atoms (**Table S3 and Figure S14**) resulting in the enhanced local concentration of CO* at the surface of the Ag-doped Cu(100) catalyst and advantageous C-C coupling. These findings suggest that the Ag atoms play the following two key roles. i) facilitating the reduction of CO_2 to CO and ii) expediting the C-C coupling by spilling over the CO atom to this asymmetrical active site with reduced transition state energy.

5.2.4. Ethanol, ethylene, and acetic acid pathways

The lowest energy pathways identified for ethanol, ethylene, and acetic acid production are illustrated in **Figure 6B-C**. All the intermediates before the C-C coupling are the same for these three products, i.e., CO_2 ⟶ *COOH ⟶ *CO ⟶ *CHO ⟶ *CO-CHO. Because of the lower TS barrier, all the elementary steps after C–C coupling are investigated based on the *CO-CHO intermediate. Acetic acid path bifurcates at the sixth coupled proton-electron step, while ethanol and ethylene share six-coupled proton-electron transfer and bifurcate only at the seventh reduction step. The common intermediate for ethanol and ethylene, i.e., *OCH-CHO*, (labeled **7A)** is more favored than the acetic acid intermediate (labeled **7B)**, indicating that the formation of ethanol and ethylene would occur before acetic acid (**Figure 6C**). This mechanistic understanding supports the experimental finding shown in **Figure 5B**, in which ethylene and ethanol are the major products and a negligible amount of acetate/acetic acid is formed from CO_2RR. However, the formation of acetate from CORR is equivalent to the formation of ethylene and ethanol (**Figure 5E**). This can be due to the presence of a high amount of CO on the catalyst surface that expedites the C-C coupling step and thereby enables the formation of other C_2 products including the acetate/acetic acid. As shown in **Figure 6**, the free energy of the acetic acid formation step (labeling **7B**) is slightly higher (0.19 eV) than those of the ethanol and ethylene (labeling **7A**) and thus, the acetic acid/acetate pathway would be feasible as well. Comparing ethanol and ethylene (which both are 12-electron reduction products), free energy diagram analysis demonstrates that ethanol formation is favored over ethylene (labeling **8a** and **8b** in **Figure 6B**, respectively). This agrees with the slightly higher percentage of ethanol over ethylene in the experimental result as shown in **Figure 5B** for the AgCu SANP.

To get further insight into the impact of Ag doping on the electronic structure of copper surfaces, we analyzed the density of states (DOS) of the pure Cu and Ag-doped Cu surfaces (in the absence of

adsorbate). In **Figure S13**, we analyze the *d*-band, which has shown to be a good descriptor to understand the differences in catalytic activities.[86] This analysis shows that the *d*-band center in pure Cu(100) surface is shifted to lower values in the Ag-doped Cu, as indicated by the vertical dashed lines. This downshift originates from the excess of DOS in Ag-doped Cu (compared to pure Cu) concerning the Fermi level. The projected DOS on the *d* orbitals of the Cu (B) atoms near the active Cu active site and Ag atom (before and after Ag substitution, respectively) also shows a downshift of the *d*-band center upon Ag substitution. The downshift of the *d*-band center in the Ag-doped Cu surface indicates that Ag reduces the bonding strength of the adsorbate at the surface, which is consistent with the weak adsorption of CO on the Ag-doped Cu surface, and the reduced reaction barriers to producing ethanol, ethylene and acetic acid molecules (**Figure 6A-B**).

5.2.5. Conclusions

In conclusion, a novel AgCu SANP cascade catalyst has been developed and exhibited a record high FE of 94% toward multicarbon products under ~720 mA cm^{-2} working current density in a flow cell. DFT calculations indicate that the high C_{2+} selectivity is ascribed to the synergistic catalysis of Ag NP and AgCu SAA in the AgCu SANP, namely Ag NP generating CO and AgCu SAA promoting the C-C coupling step. This work not only develops a highly effective catalyst for multicarbon products production but also provides a new cascade catalysis strategy for future C_{2+} selective catalyst development.

5.2.6. Methods

Chemicals: All solvents, unless otherwise mentioned, are ACS grade. The water used was purified by a Milli-Q system with a resistivity of 18.2 MΩ cm. All pure gasses, for electrocatalysis and gas chromatography, were obtained from Praxair and Linde with the associated purities, CO_2 LaserStar 5.0 (99.999%), Air Zero (maximum 3ppm water, 1 ppm total hydrocarbons), Helium 5.5 (99.9995 %), Hydrogen 5.5 (99.9995%), Argon 5.0 (99.9995%). The gas mixture for GC calibration (Supelco 23462) was obtained from Sigma-Aldrich. For NMR tests, deuterium oxide (99.9 atom % D), dimethyl sulfoxide (99.5%), formic acid (98%), and 1-propanol (99.9%) were obtained from Sigma Aldrich. Ethylene glycol was obtained from VWR Chemicals (laboratory grade), and 100 nm copper nanoparticles and silver nitrate (99%) were obtained from Sigma Aldrich. Nafion 117 containing solution (~5% in a mixture of lower aliphatic alcohols and water) was obtained from Sigma Aldrich. Sigracet 36BB gas diffusion electrodes were purchased from the Fuel Cell Store. Nickel foam (99.9%) was purchased from MTI Corporation. Potassium hydroxide (85%) was obtained from Sigma Aldrich.

Synthesis of AgCu SANP: 20 mg Cu NPs and 2 mg $AgNO_3$ were firstly dispersed into 5mL ethylene glycol and 0.2mL H_2O, respectively. Then, the two solutions were combined being together and put in an ultrasonic bath for the galvanic reaction for 30 min. After that, the nanoparticles were washed with water and isopropanol and collected using the centrifuge. The obtained nanoparticles contain both Ag single-atoms and nanoparticles, labeled as AgCu SANP. The AgCu SAA and AgCu NP were prepared using a similar method, except for the different $AgNO_3$ usage (0.1 mg for AgCu SAA and 20 mg for AgCu NP).

Preparation of GDE: AgCu-based nanoparticles were firstly dispersed into IPA with a concentration of 5 mg mL^{-1}. The Nafion-117 solution was also added to the IPA solution with 1% volume. After mixing under ultrasound conditions for 30 min, the catalyst ink was directly sprayed on the GDL (Sigracet 36 BB) using an airbrush. The final loading of GDE was determined by balancing the weight difference before and after the airbrush step, which was about 0.5 mg cm^{-2}.

Material characterization: Scanning electron microscopy (SEM) images were captured on a Hitachi S4800 with a working accelerating voltage of 10 kV. Glancing-incidence X-ray diffraction (GIXRD) was measured on a PANalytical X'Pert Pro MRD diffractometer with Cu Kα radiation (1.54 Å) at an incidence angle of 0.3°. X-ray photoelectron spectroscopy (XPS) measurements were carried out on a Thermo-VG Scientific ESCALab 250 microprobes with a monochromatic Al Kα X-ray source (1486.6 eV). The obtained spectra were calibrated using the C 1s line. Aberration-corrected scanning transmission electron microscope (AC-STEM) tests were carried out on an FEI Titan 80-300 HB TEM equipped with energy-dispersive X-ray spectroscopy (EDS) at 200 kV. The HAADF-STEM images were recorded by FEI Titan 80-300 HB TEM/STEM with an aberration corrector operating at 300 kV. Inductively coupled plasma-atomic emission spectrometry (ICP-MS) tests were carried out on X Series quadrupole, Thermo Scientific USA. Proton nuclear magnetic resonance (H-NMR) was measured on Bruker Avance III 300 MHz. GC tests were conducted on an Agilent 6890 machine with Carboxen (TCD) and Carbonplot (FID) columns. XAS measurements were carried out at the Advanced Photon Sources (APS) 20-ID-C and 20-BM beamlines. The measurements at the copper K-edge and Ag K-edge were performed in fluorescence mode using a Lytle detector. The XAS data were analyzed using the software package Athena.

Electrochemical CO_2RR measurements: All electrochemical tests were measured on Gamry Reference 3000 electrochemical workstation at room temperature with IR compensation. A three-electrode system was fabricated with the prepared AgCu-based GDE, Ni foam, and Ag/AgCl electrode severing as working electrode, counter electrode, and reference electrode, respectively. A gas-tight, three-chamber flow cell equipped with a piece of Fumasep FAB-PK-130 anion exchange membrane (AEM) was employed to

conduct the electrochemical reaction. Before CO_2RR tests, the AEM was firstly activated in 1M KOH solution for 12h. The CO_2RR catalytic activities were evaluated using the potentiostatic technique under selective potential for 10 min in 1M KOH with flowing pure CO_2 gas. The flow rate of electrolyte and CO_2 gas was 18 mL min^{-1} and 30 sccm, respectively. All the potential values are relative to the RHE unless otherwise stated. The gas products were tested using online GC, liquid products are detected using H-NMR.

Determination of gas products using GC method: Standard curves of CH_4, CO, C_2H_2, C_2H_4, and C_2H_6 gases was firstly built using standard gas. In detail, different concentrations were prepared by diluting the mixture with CO_2 using mass flow controllers (Alicat Scientific). The produced standard curves are shown in Figure S7. During the electrocatalytic CO_2 reduction, the gas products flow into the GC with the input CO_2 gas in the online tube. In experiments, CH_4 and C_2H_4 are the main gas products that can be detected in the flame ionization detector (FID), and CO was detected by the thermal conductivity detector (TCD).

Determination of liquid products using the NMR method: Standard curves of ethanol, formate, acetate and propanol was firstly built using pure chemicals with known concentrations. NMR tubes were prepared by combining 70 μL D_2O and 30 μL of aqueous 5 mM DMSO internal standard with 630 μL of sample. The produced standard curves are shown in Figure S8. After electrocatalytic CO_2 reduction, the electrolyte was collected and mixed with the NMR detecting solution (DMSO internal standard DMSO, D2O, as above). For H-NMR tests, 128 scans were performed, with excitation sculpting used to suppress the water peak. As presented in Figure S8, ethanol, formate, acetate, propanol, and DMSO can be ascribed to the peaks located at 1.07 (triplet) and 3.55 (quartet), 8.35 (singlet), 3.44 (triplet), and 1.42 (sextet) and 0.77 (triplet), and 2.61 ppm, respectively. Signals from the OH proton in the alcohols are not observed, which is likely due to hydrogen-deuterium exchange.

DFT Calculations: All DFT calculations have been performed using the Vienna ab initio simulation package (VASP) with spin polarization [87]. The generalized gradient approximation (GGA) exchange-correlation functional parametrized by Perdew, Burke, and Ernzerhof (PBE) for the electronic interactions, and the projector-augmented wave (PAW) method for the core electrons was used [88, 89]. A cutoff energy of 600 eV was used for the plane wave. The convergence criterion for the electronic self-consistent iteration was set at 10^{-6} eV. During the relaxation, we assumed the relaxation was achieved when the atomic forces were lower than 0.05 eV/Å. We used a Monkhorst−Pack grid with dimensions of 4×4×1 for sampling the first Brillouin zones [90]. The DOS calculations were done using a 12 × 12 × 12 *k*-points grid, and the tetrahedron method with Blöchl correction [91]. The *d*-band center was calculated with an integration

window of -10 to 10 eV. The copper surface was modeled using 2 × 2 supercells of the fcc(100) with four layers, for which only the bottom two layers were frozen, while the rest of the system was allowed to relax. The Cu(100) is doped with Ag by substituting one Cu atom with Ag, which corresponds to a 3% Ag doping concentration on the Ag-doped Cu surface. To ensure that the interactions between neighboring periodic images are negligible, a vacuum region along the z-direction has been added so that the distance between the two nearest surface atoms in neighboring images is at least 16 Å. We employed the DFT-D3 Grimme method for long-range dispersion interaction correction.[92] For the C-C coupling, a transition state search was carried out by automated relaxed potential energy surface scans (ARPESS) [93]. The computational hydrogen electrode (CHE) model proposed by Nørskov et al. was used to calculate the free energies of CO_2 reduction intermediates, based on which the free energy of an adsorbed species is defined as $\Delta G_{\text{ads}} = \Delta E_{\text{ads}} + \Delta E_{\text{ZPE}} - T\Delta S_{\text{ads}} + \int C_{\text{P}}\mathrm{d}T$, where ΔE_{ads} is the electronic adsorption energy, ΔE_{ZPE} and $T\Delta S_{\text{ads}}$ represent zero-point energy and entropy (difference between adsorbed and gaseous species), respectively, $\int C_{\text{P}}\mathrm{d}T$ is the enthalpy correction and *T* is at room temperature [94].

5.2.7. Acknowledgment

Y.A.W. thanks the funding from the National Research Council of Canada Materials for Clean Fuels Challenge Program (CH-MCF-123), and the Natural Sciences and Engineering Research Council of Canada (NSERC) (RGPIN-2020-05903, GECR-2020-00476). This research used resources of the Advanced Photon Source, an Office of Science User Facility operated for the U.S. Department of Energy (DOE) Office of Science by Argonne National Laboratory and was supported by the U.S. DOE under Contract No. DE-AC02-06CH11357, and the Canadian Light Source and its funding partners.

5.3. Supporting Information

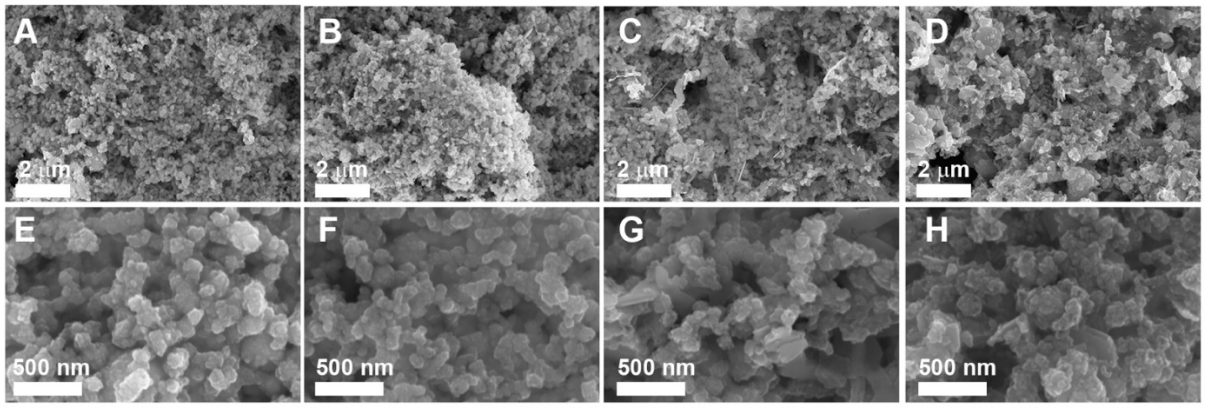


Figure S1. *SEM images of Cu NP (A and E), AgCu SAA (B and F), AgCu SANP (C and G), and Ag NP (D and H).*

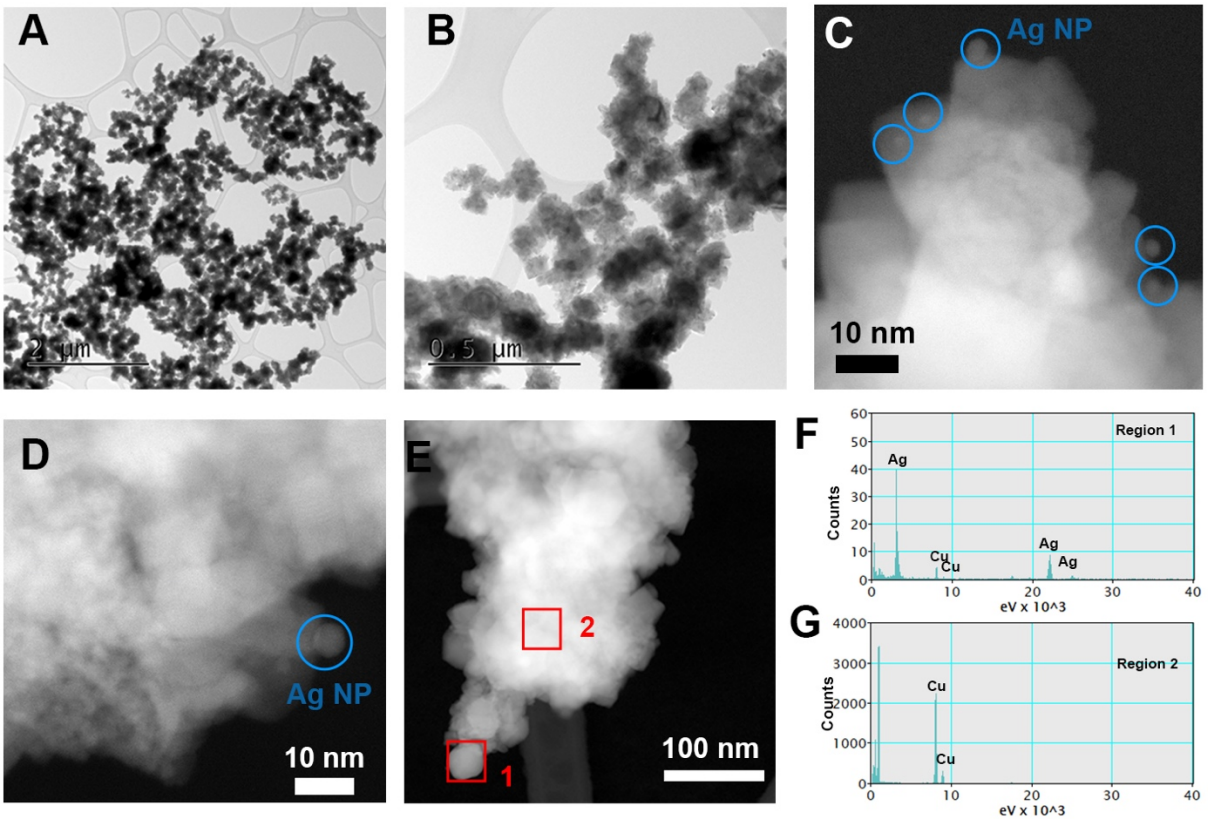


Figure S2. *(A-B) BF-STEM images of AgCu SANP; (C-D) HAADF-STEM images of AgCu SANP, the representative Ag NP are marked by the circle; (E) HAADF-STEM image of AgCu SANP, region 1 represents the Ag NP, region 2 represents AgCu SAA; (F) EDX of region 1, which shows the apparent signal of Ag and Cu; (G) EDX of region 2, which only shows the signal of Cu without Ag due to the low content of Ag in AgCu SAA composition.*

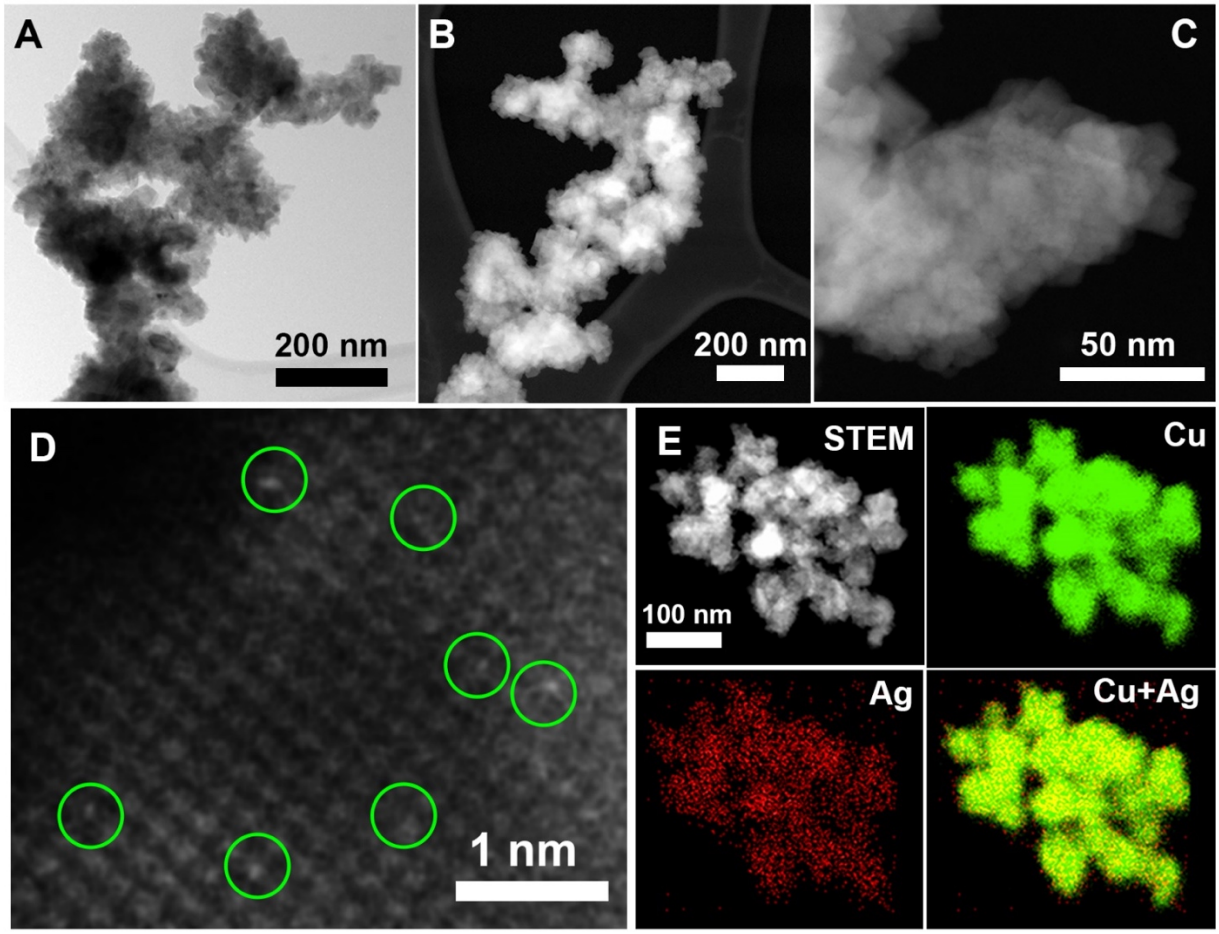


Figure S3. *(A) BF-STEM image of AgCu SAA; (B-C) HAADF-STEM images with different magnifications of AgCu SAA; (D) AC-HAADF-STEM image of AgCu SAA, the bright dot marked by the circle represents the Ag single-atoms; (E) STEM and EDS element mapping images of AgCu SAA.*

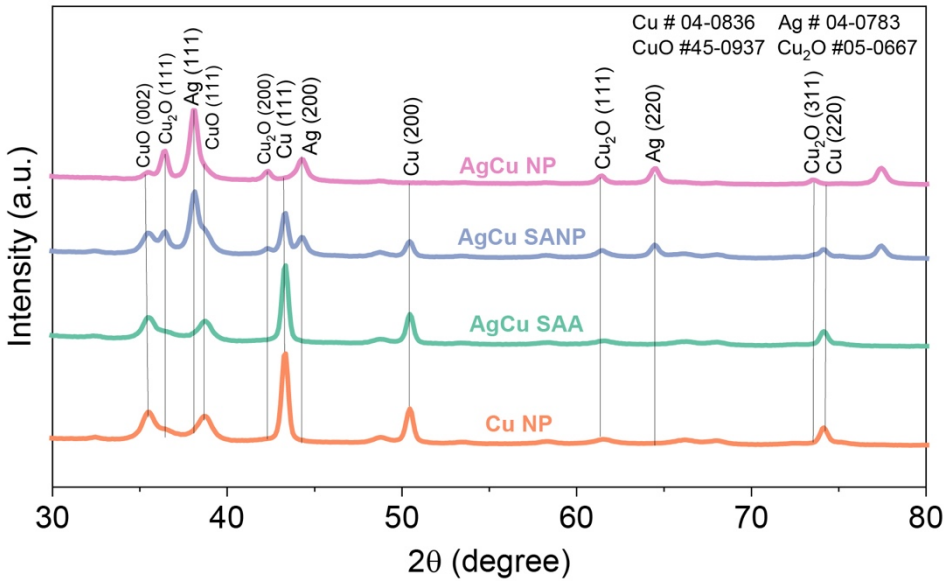


Figure S4. *XRD spectra of Cu NP, AgCu SAA, AgCu SANP and AgCu NP.*

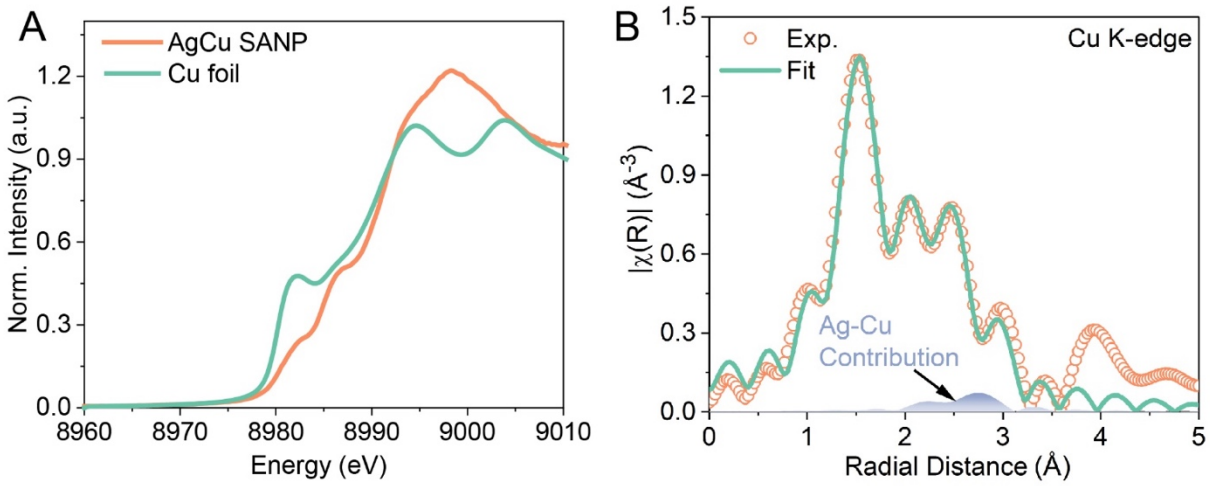


Figure S5*. (A) Cu K-edge XANES spectra of AgCu SANP and Cu foil; (B) Ag K-edge EXAFS experimental and fitting spectrum of AgCu SANP.*

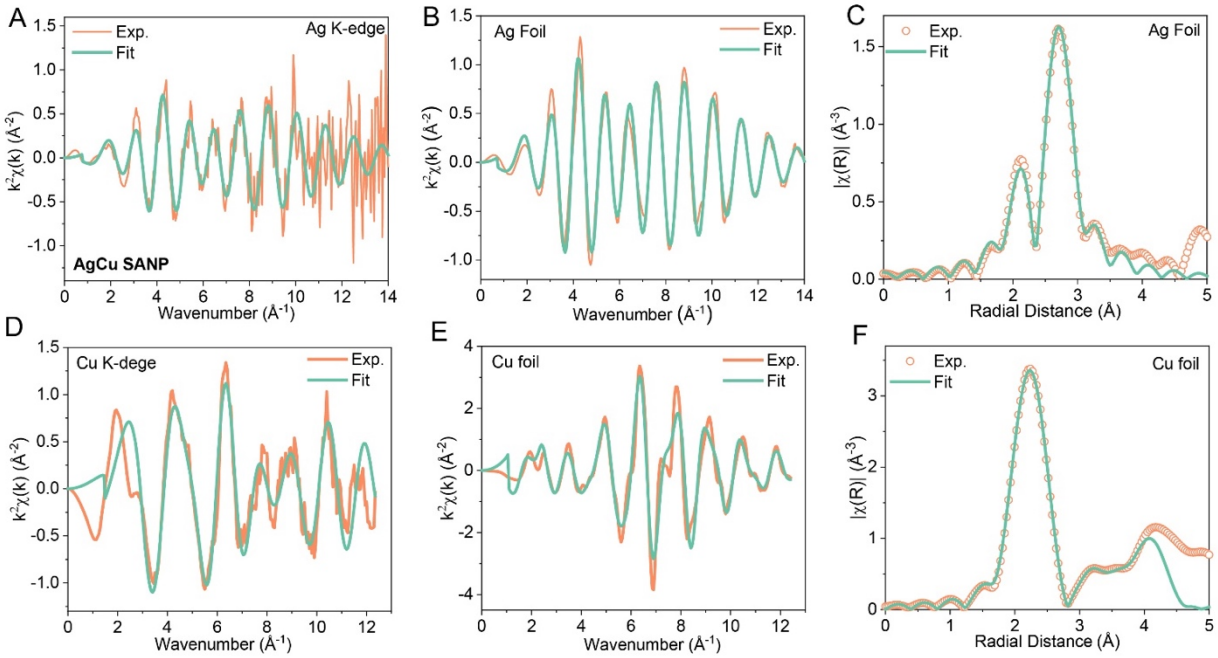


Figure S6*. (A-B) Experimental and fitting spectra of Ag K-edge in k space of AgCu SANP (A) and Ag foil (B); (C) Experimental and fitting spectra of Ag K-edge in r space of Ag foil; (D-E) Experimental and fitting spectra of Cu K-edge in k space of AgCu SANP (D) and Cu foil (E); (F) Experimental and fitting spectra of Cu K-edge in r space of Cu foil*

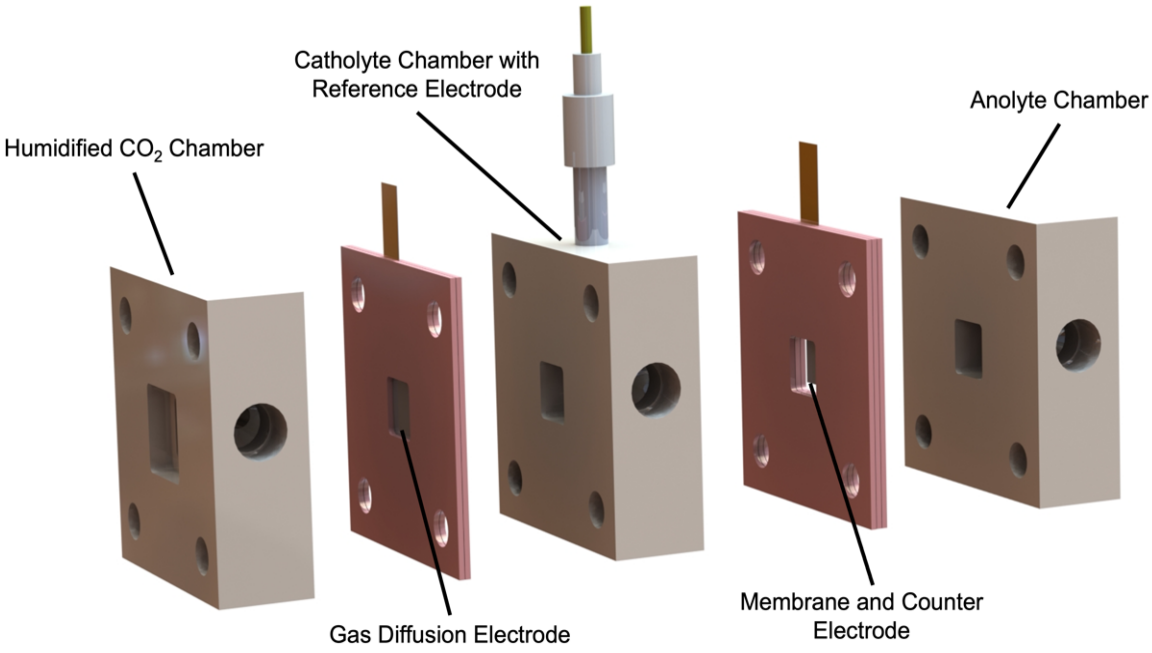


Figure S7*. Schematics of the flow cell.*

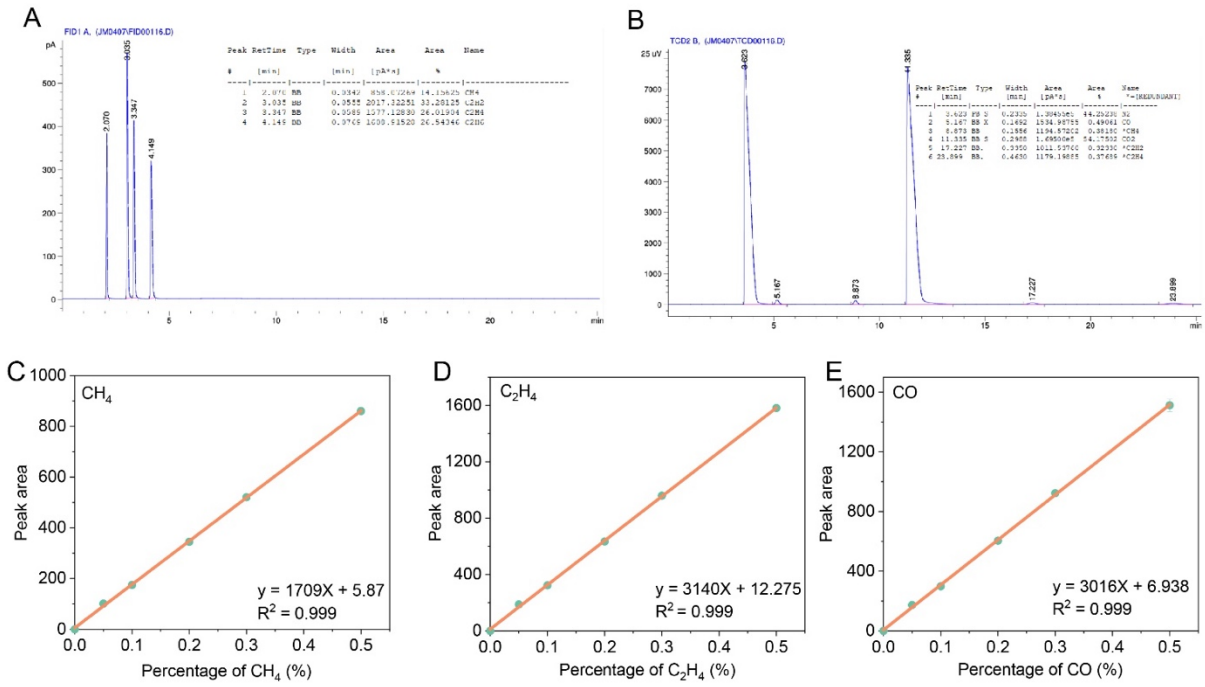


Figure S8. *(A) Representative gas chromatography (GC) flame ionization detector (FID) spectrum for CO_2RR products; (B) Representative GC thermal conductivity detector (TCD) spectrum for CO_2RR products; (C-D) Standard curves of CH_4 (C), C_2H_4 (D), and CO (E).*

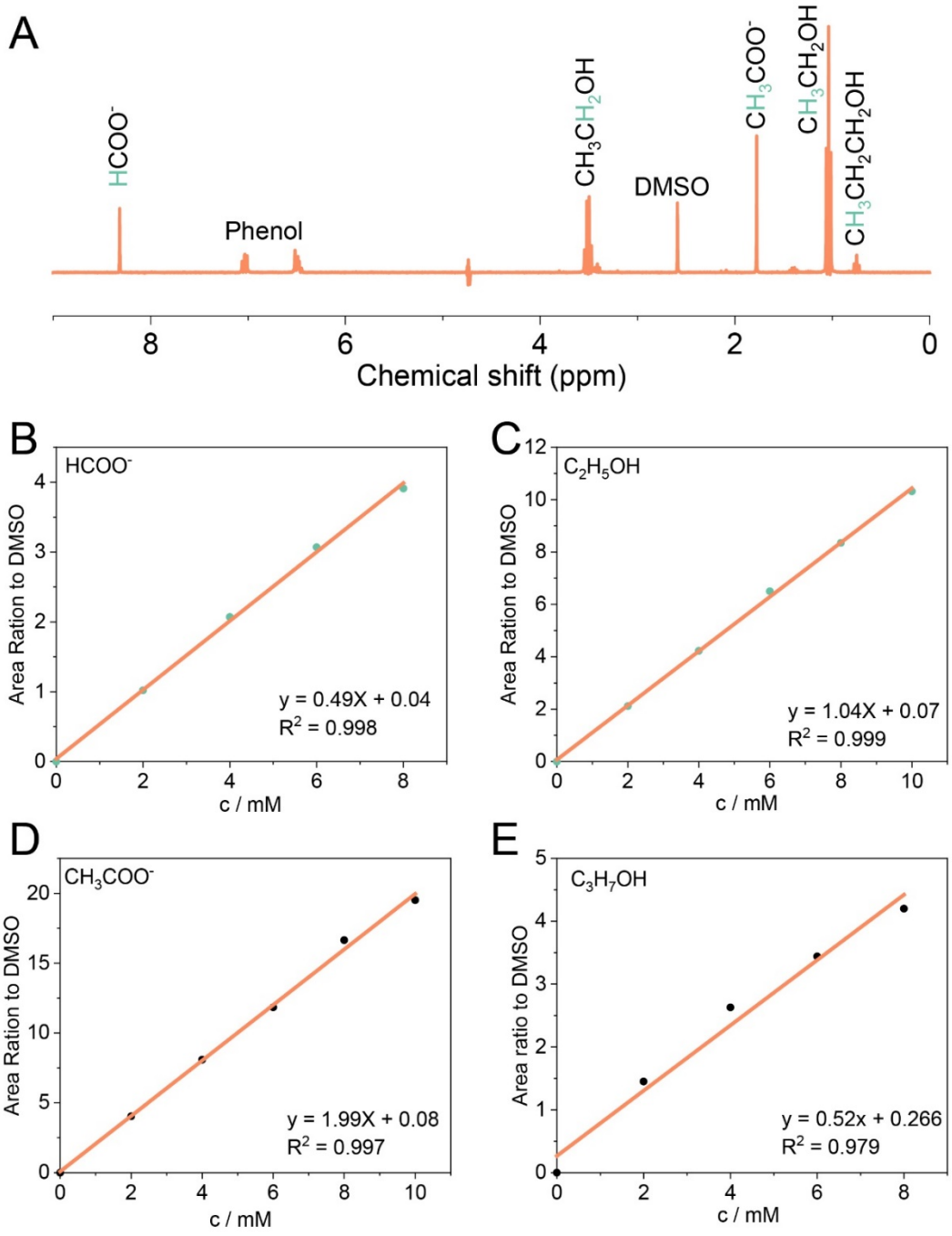


Figure S9. *(A) Representative NMR spectrum for CO_2RR products; (B-E) Standard curves of $HCOO^-$ (B), C_2H_5OH (C), CH_3COO^- (D) and C_3H_7OH (E).*

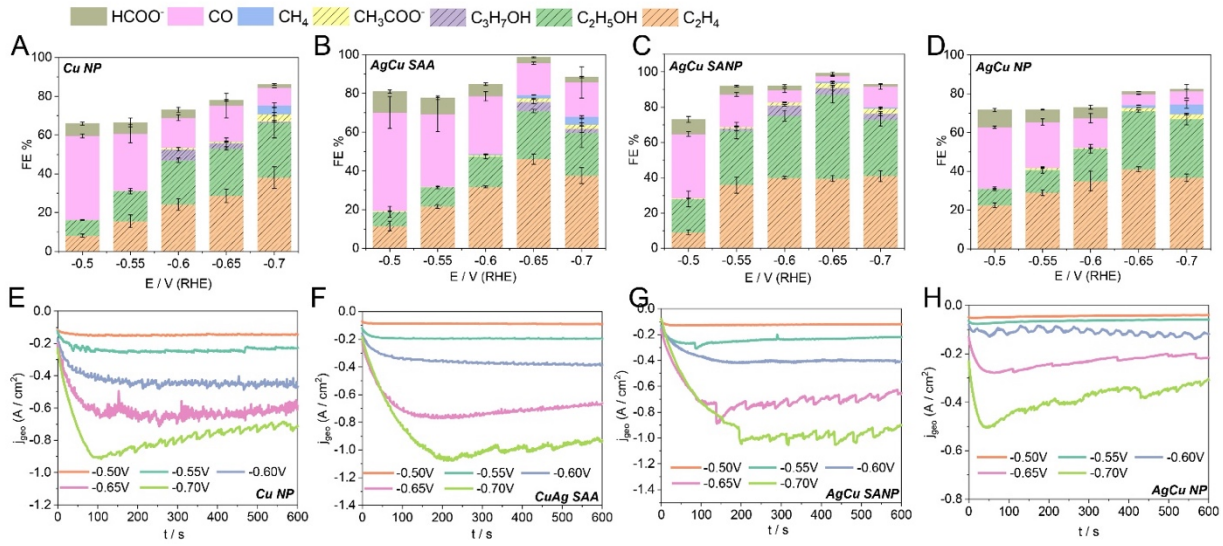


Figure S10. *(A-D) Faradic efficiency (FE) results of Cu NP, AgCu SAA, AgCu SANP, and Ag NP under different potentials; (E-H) I-t curves of Cu NP, AgCu SAA, AgCu SANP, and Ag NP under different potentials.*

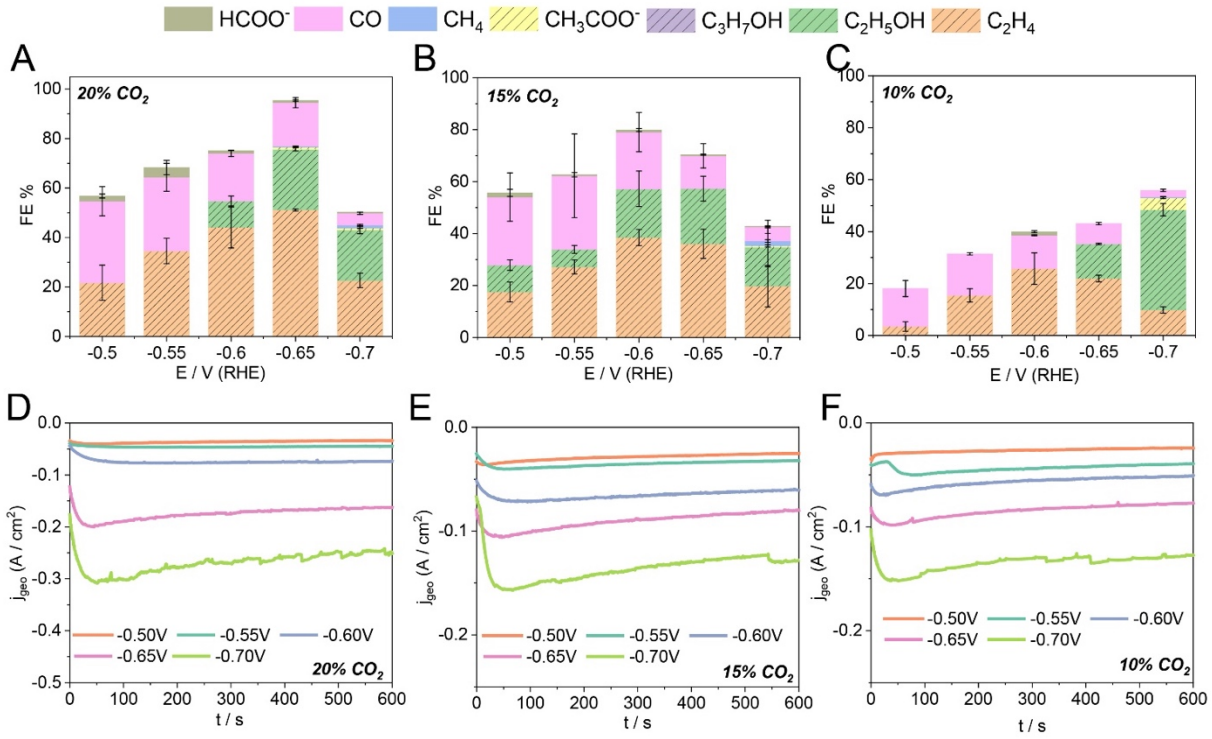


Figure S11. *(A-C) FE results of AgCu SANP for CO_2RR feeding with different CO_2 concentrations, 20% (A), 15% (B) and 10% (C); (D-F) I-t curves of AgCu SANP for CO_2RR feeding with different CO_2 concentrations, 20% (D), 15% (E) and 10% (F).*

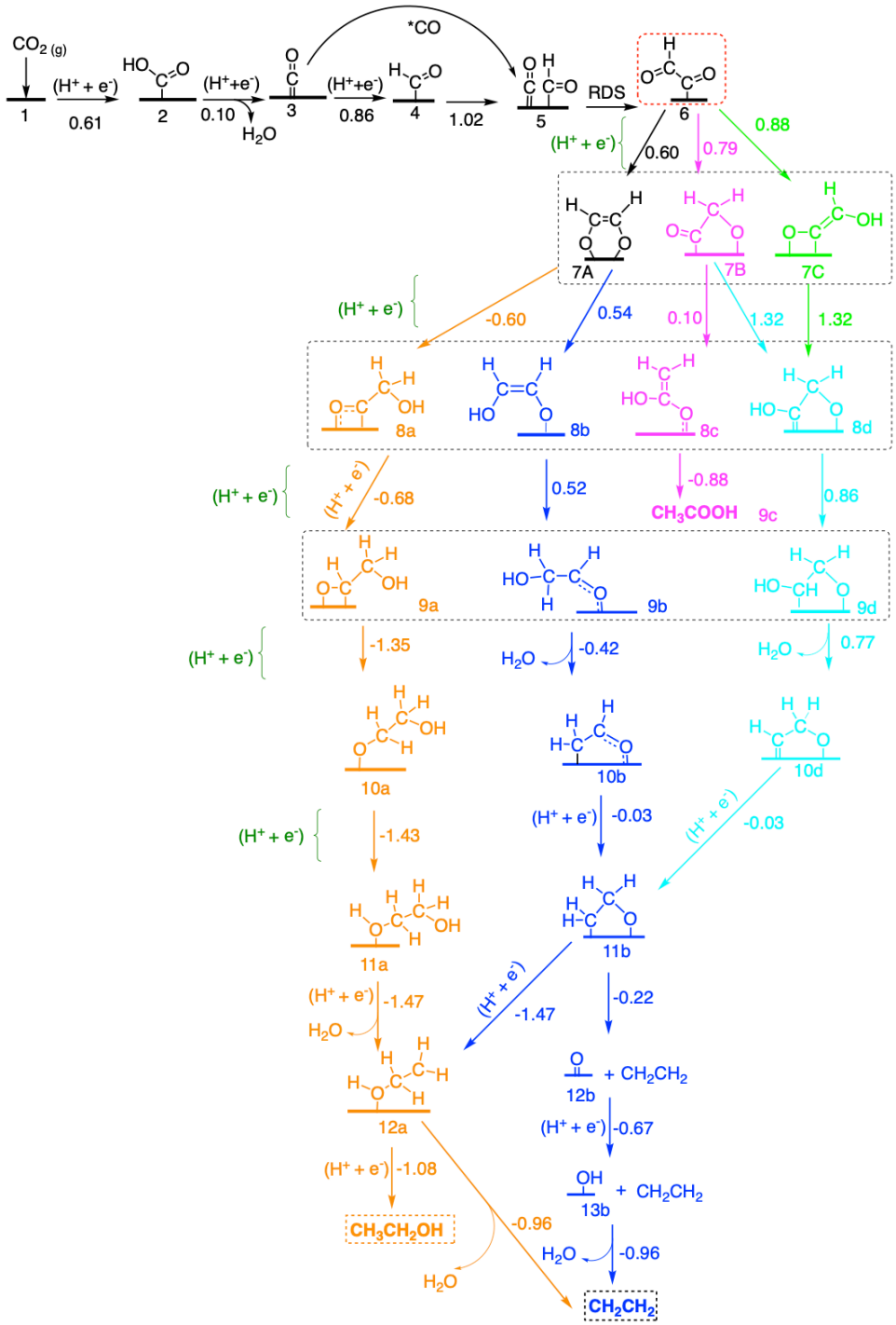


Figure S12. *Proposed all mechanistic pathways for the formation of ethanol, ethylene, and acetic acid. The most less energetic pathways are given in the main text. The free energy of the reactions indicated in the arrows is in eV. Courtesy of Professor Samira Siahrostami, Dr. Asfaw Yohannes, Dr. Jian Xiang Lian at the University of Calgary.*

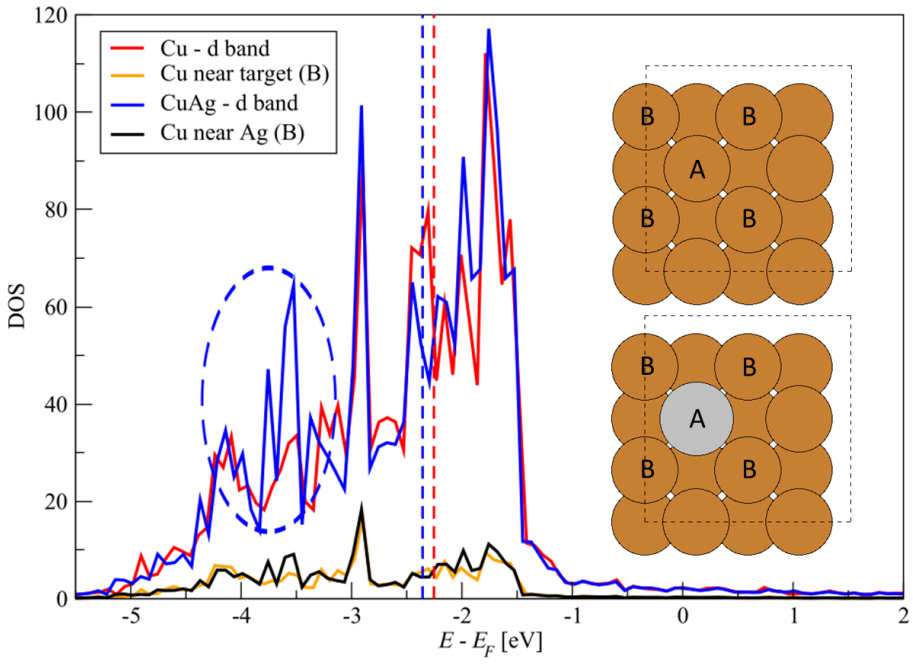


Figure S13. *Projected d-band for pure Cu (red and orange lines) and Ag-doped Cu (blue and black lines) surfaces. Orange and black lines are the DOS projected on the d-band of the atoms near the target Cu (in pure Cu) and Ag atom (in CuAg). Insets: the target Cu and Ag atoms are indicated with the label 'A' whereas the first-neighbor Cu atoms are indicated with 'B'. The red and blue dashed lines indicate the d-band center of the pure Cu and CuAg surfaces, respectively. The Blue dashed oval indicates the excess DOS in CuAg. Courtesy of Professor Samira Siahrostami, Dr. Asfaw Yohannes, Dr. Jian Xiang Lian at the University of Calgary.*

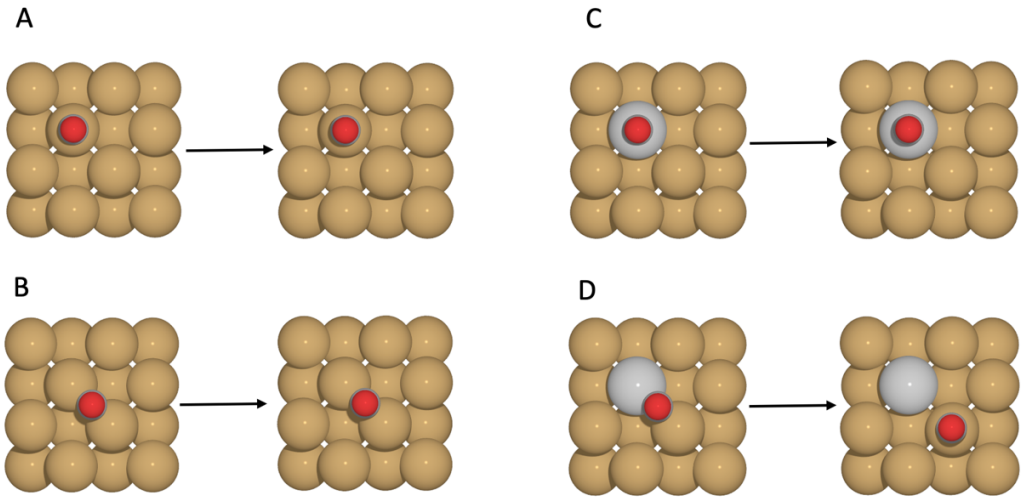


Figure S14. *CO adsorbed structures before and after optimization for the ontop and bridge sites on pure Cu surface (A and B, respectively) and on Ag doped-Cu surface (C and D, respectively). Courtesy of Professor Samira Siahrostami, Dr. Asfaw Yohannes, Dr. Jian Xiang Lian at the University of Calgary.*

***Table S1**. Fitted EXAFS parameters at the Cu and Ag K-edge for AgCu SANP, Ag foil, and Cu foil*

AgCu SANP	CN	error	R(Å)	ERROR	E_0(eV)	σ^2(Å^2)	R-factor
Ag-Ag	7.32	0.73	2.859	0.009	2.4(7)	0.0080(1)	0.0103
Ag-Cu	1.03	0.09	**2.810**	0.048		0.0125(9)	
AgCu SANP	CN	error	R(Å)	ERROR	E_0(eV)	σ^2(Å^2)	R-factor
Cu-O	2.12	0.36	1.952	0.170	8(2)	0.0019(5)	0.0204
Cu-O	1.06	0.18	2.689	0.077		0.0030(2)	
Cu-Cu(oxide)	2.12	0.36	3.076	0.042		0.0118(1)	
Cu-Cu(metal)	1.42	0.65	2.548	0.018		0.0012(8)	
Cu-Ag	0.95	0.09	2.810	0.048		0.0008(5)	
Ag_foil	CN	error	R(Å)	ERROR	E_0(eV)	σ^2(Å^2)	R-factor
Ag-Ag	12		2.866	0.003	2.1(3)	0.0092(4)	0.0021
Cu_foil	CN	error	R(Å)	ERROR	E_0(eV)	σ^2(Å^2)	R-factor
Cu-Cu	12.00		2.544	0.003	4.5(5)	0.0090(4)	0.0011
Cu-Cu	6.00		3.595	0.022		0.0148(4)	
Cu-Cu-Cu	48.00		3.848	0.046		0.0202(5)	
Cu-Cu-Cu	48.00		4.373	0.032		0.0032(5)	
Cu-Cu	24.00		4.418	0.018		0.0125(2)	

CN: coordination number; R: distance; E_0: energy shift; σ^2: mean-square disorder; R-factor: goodness of EXAFS fitting). The numbers in the parentheses are the last digit error.

***Table S2**. Performance comparison of AgCu SANP and reported results in Figure 3D*

Catalyst	NO.	j_{total} mA cm^{-2}	C_{2+} FE	Reference
AgCu SANP	1	720	94	This work
$La_{2-x}CuO_{4-\delta}$	2	51.3	41.5	Angew.Chem.Int.Ed., 2022, 61, e202111670
$Cu_xO_yC_z$	3	80	54	Angew. Chem. Int. Ed., 2021,60,23427–23434
Cu-PzH	4	346	60	Angew. Chem. Int. Ed., 2021,60,19829–19835
alkanethiol-modified Cu	5	255	64	J. Am. Chem. Soc. 2021, 143, 21, 8011–8021
CuO/Al_2CuO_4	6	600	70.1	Energy Environ. Sci., 2022, DOI: 10.1039/d1ee03861c
F-Cu	7	400	70.4	Green Chem., 2022, DOI: 10.1039/D1GC04824D
Cu-CuI	8	700	71	Angew. Chem. Int. Ed., 2021,60, 14329-14333
$Cu_2P_2O_7$	9	350	73.6	Angew. Chem. Int. Ed.2022,61,e202114238
Cu-SiO_x	10	300	75	Nat. Commun., 2021,12:2808
electrodeposited Cu	11	150	75	J. Am. Chem. Soc., 143(8), 3245-3255.
Cu_3-Ag_3Au	12	230	77	Angew.Chem.Int.Ed.2021, 60,2508–2518

B-Cu-Zn	13	200	79	Angew. Chem. Int. Ed., 2021, 60(16): 9135-9141.
Cu NPs with +1 valence	14	300	80	Adv. Energy Mater. 2021, 2101424
CuNi	15	250	80.5	ACS Materials Lett. 2021, 3, 1143−1150
Cu@Pb	16	400	81.6	ACS Nano 2021, 15, 1, 1039–1047
Cu_3N_x	17	307	81.7	Adv. Mater. 2021, 2103150
Cu Nanoribbons	18	347.9	82.3	Adv. Energy Mater. 2021, 11, 2102447
Oxide-Derived Copper	19	341.5	83.8	Chem. Sci., 2021, DOI: 10.1039/D1SC00042J
SHKUST-1	20	400	88.4	Angew. Chem. Int. Ed., 2022, 61(2): e202111700.
$Cu(OH)_2$-derived Cu	21	217	87	Angew.Chem.Int.Ed.2021, 60,4879 –4885
N-C/Cu	22	300	93	Nat. Energy, 2020, 5(6): 478-486

***Table S3**. Gibbs free adsorption energies (ΔG_{ads}) of CO on Ag doped-Cu surface and pure Cu surface. CO adsorption on the bridge between Cu-Ag and 4-fold hollow sites is not stable (migrates to the nearby Cu sites). Courtesy of Professor Samira Siahrostami, Dr. Asfaw Yohannes, Dr. Jian Xiang Lian at the University of Calgary.*

Ag doped-Cu surface		Pure Cu surface	
Site type	ΔG_{ads} (eV)	Site type	ΔG_{ads} (eV)
Ontop of Cu	-0.60		
Ontop of Ag	-0.18	Ontop	-0.85
Bridge Cu-Cu	-0.63	Bridge	-0.87
Bridge Cu-Ag	unstable	Hollow (4-fold)	-0.90
Hollow (4-fold)	unstable		

Chapter 6

6. Synthesizing High-Entropy Alloys for Electrochemical CO_2 Conversion

6.1. Introduction

Electrochemical CO_2 conversion into fuels and feedstocks has the potential to provide a form of energy storage for intermittent renewable energy sources and to provide carbon storage for atmospheric CO_2. Currently, while there has been significant progress in this field, effective catalysts are in lack for electrochemical CO_2 conversion to multicarbon products. Detailed examples are provided in earlier chapters.

In this work, we investigate the making of novel alloy materials. Alloying is a method used to produce new materials by mixing at least two metallic elements to form a solid solution. Miscibility is generally a requirement for alloying as not any arbitrary combination of elements can form a homogeneous solution, neither for robust tuning of the ratio between the two components. Using this electro-shock method of thermal processing, we combine five different elements to form a single phase HEA nanoparticles.

6.2. Catalyst Synthesis

The catalyst material synthesis begins with activation of carbon black in nitric acid according to [95]. This step introduces oxygen functional groups on the surface of the carbon nanoparticles. Once activated, the product is washed with water and collected by centrifuge. Then, ink mixtures are prepared by mixing the carbon nanoparticles with transition metal salt solutions. Different combinations of the following elements dissolved at a concentration of 0.01 M in ethanol, are combined: $CuCl_2$, $AgNO_3$, HAuCl4, $ZnCl_2$, $NiCl_2$, $CoCl_2$, $FeCl_3$ (all ACS grade or higher, Sigma-Aldrich). The ink is sprayed onto a piece of 1 cm wide by 3 cm long CT Carbon Cloth by an airbrush.

Once the mixture is allowed to dry, 10 A current is passed through the sample for a duration of 0.1 s. During this time, the temperature is elevated and melts the salts on the electrode. The temperature falls rapidly, giving a quench effect. The metals solidify into a solution, with the elements distributed throughout. This technique follows a previous method [96].

6.3. Results and Discussion

Synthesized catalyst nanoparticles are pictured in **Figure 7**. According the SEM images, we confirmed the electro-shock method to break through the immiscible limitation. This method can synthesize nanoscale homogeneous alloys materials. A single homogeneous solid solution forms that allows for the incorporation of earth-abundant transition metals atoms at various ratios and in a particle of nanometer-size. The high-entropy alloy nanoparticles are believed to have great potential for tuning the CO_2 reduction reaction.

However, preliminary performance testing has not yet yielded meaningful CO_2 conversion. Fortunately, the combinations and ratios of possible metal salts are limitless, which makes the optimization of the catalyst for this reaction simultaneously difficult and promising. It is hoped that this approach to catalyst design will yield high-performance catalyst materials for CO_2 reduction.

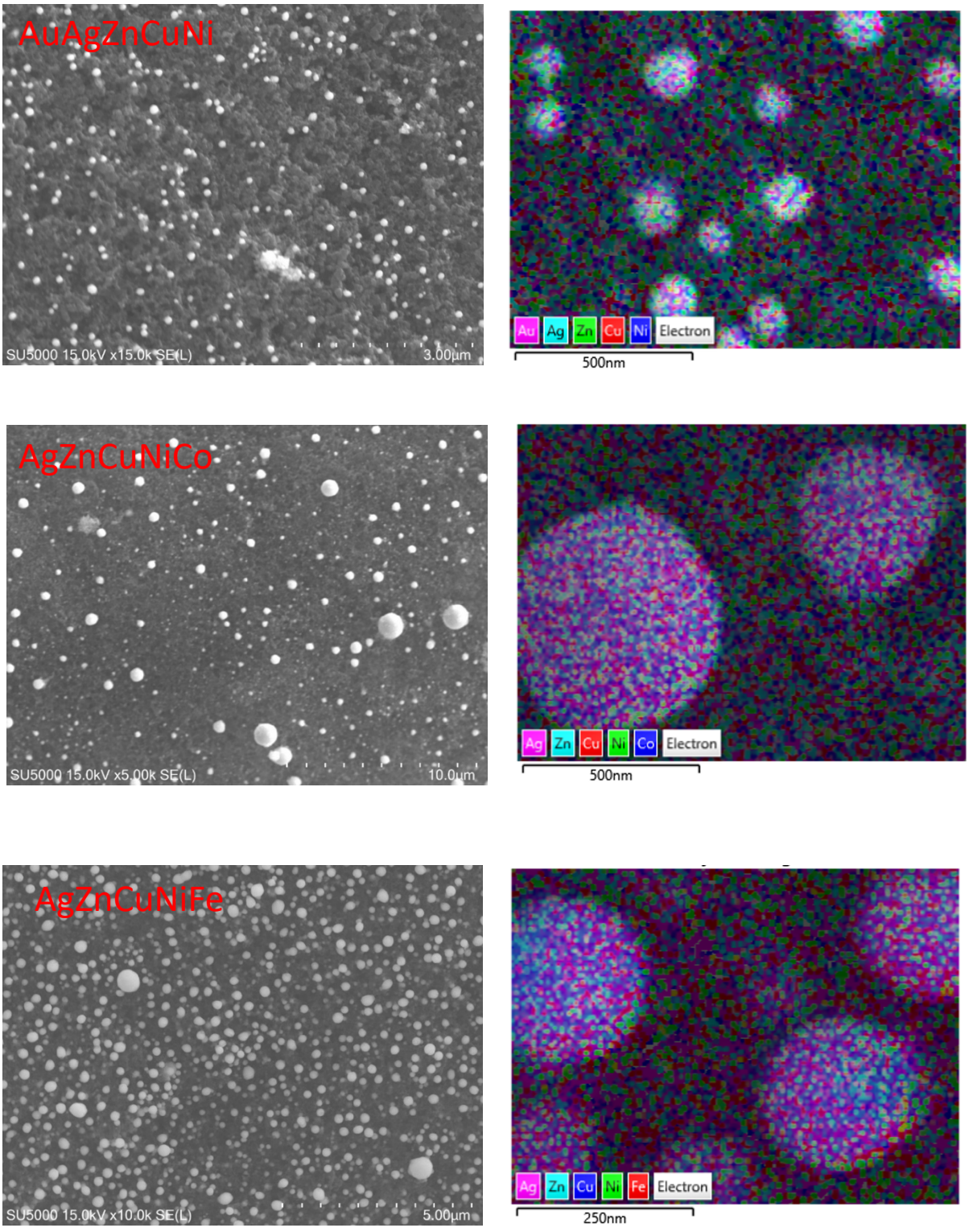


***Figure** 7. Scanning electron microscope images (left) and corresponding elemental mapping (right) of selected high-entropy alloy samples. Constituent elements are labelled on each image.*

6.4. Next Steps

With the synthesis procedure of high-entropy alloy nanoparticles fully developed, the next steps are to continue tuning the elements and ratios of elements. Rather than approximately equal ratios of each element, the next approach is to revert to a copper-dominant strategy, knowing its ability to catalyze the conversion of CO_2 into multicarbon products. By tuning the catalyst composition, high-performance catalysts should be obtained.

Once a high-performance material is discovered, the next step is to develop a mechanistic understanding of its performance. When done comprehensively, this entails in-situ characterizations of the catalyst and identification of the reaction intermediates. Coupling this data with DFT calculations can give a concrete picture of the catalyst features driving the catalyst's performance.

Chapter 7

7. Conclusions

7.1. Main Takeaways from this Work

A technoeconomic analysis of electrochemical CO_2 conversion concludes that while the economic barriers are high, the capital cost of the cell and materials, including catalysts, will play a driving role in the future viability. When considering the cost of a catalyst, the useful lifetime becomes very important because the expense can be divided across its life. Therefore, using earth-abundant materials, scalable synthesis methods, and targeting highly stable catalysts are of high importance.

In the following chapter, we present a novel cascade catalyst used for CO_2 conversion into multicarbon products. A record 94% selectivity for multicarbon products is obtained using this combination of Ag nanoparticles and Cu with distributed Ag single atoms.

A new direction is presented with high-entropy alloys. We synthesize solid solution nanoparticles with five constituent elements. While the performance results are lacking, the synthesis technique is nonetheless promising for CO_2 conversion.

7.2. Future directions

For the future, two significant areas of opportunity are (i) conversion of CO_2 into more valuable and energy-dense multicarbon (C_{2+}) products and (ii) carbon efficiency, as some of the most impressive results to date were performed in cells which compromise the carbon efficiency by allowing input CO_2 to go to waste, an easily forgotten cost. Therefore, in the following paragraphs, future research activities are proposed.

First, the synthesis of novel catalyst materials with the goal of improving CO_2 conversion performance towards C_{2+} products. The range of strategies include alloying, crystal structure design, porosity, and interface engineering. Some lessons can be learned from the catalyst material design strategies for nitrogen conversion to ammonia [97], as many of the challenges and strategies in that article also apply to this work, such as competitive hydrogen evolution and binding key reaction intermediates. Candidate materials should undergo performance testing under the most relevant conditions for commercial application.

For promising candidates, characterization of catalysts with the goal of discovering a mechanistic understanding of the interaction between the catalyst material and reaction species. This includes, as appropriate: *ex-situ* and *in-situ* transmission electron microscopy (TEM), X-ray diffraction (XRD), X-ray photoelectron spectroscopy (XPS), for catalyst size, shape, elemental composition, crystal structure and valence state, and *in-situ* Raman and X-ray absorption spectroscopy (XAS) to identify reaction intermediates and observe the chemical nature of the catalyst under reaction conditions.

Concurrently, implementation and iteration upon the state-of-the-art advanced test conditions for maximizing carbon efficiency. Going beyond the obvious control of reactor cell geometry and flow rates, pioneers in the field are converting bicarbonate, an intermediate in state-of-the-art CO_2 capture, [98] rather than gaseous CO_2 or, converting CO_2 in acidic conditions [45]. Both techniques have their own limitations, including current density and product selectivity. In concert with technoeconomic analysis (TEA) and lifecycle analysis (LCA), rational iterations on state-of-the-art techniques will be made to make the conversion of CO_2 more economically viable and environmentally responsible.

According to the technoeconomic analysis, the cost of the catalyst will prohibit some materials and processes. While the experimental-scale synthesis of novel nanostructured catalysts will always be expensive, any candidate material should have a path to scalability using earth-abundant elements. For those elements which are less abundant, or materials synthesized using difficult-to-scale methods,

reporting the utilization, in units of catalyst loading per cm^2, is of interest. Ultimately, the success of CO_2 conversion technology into fuels and feedstocks depends on the reduction of costs to the point of being cost-competitive with the traditional sources.

References

[1] S. Ó. Snæbjörnsdóttir, B. Sigfússon, C. Marieni, D. Goldberg, S. R. Gislason, and E. H. Oelkers, "Carbon dioxide storage through mineral carbonation," *Nature Reviews Earth & Environment,* vol. 1, no. 2, pp. 90-102, 2020-02-01 2020, doi: 10.1038/s43017-019-0011-8.

[2] P. De Luna, C. Hahn, D. Higgins, S. A. Jaffer, T. F. Jaramillo, and E. H. Sargent, "What would it take for renewably powered electrosynthesis to displace petrochemical processes?," *Science,* vol. 364, no. 6438, p. 350, Apr 26 2019, doi: 10.1126/science.aav3506.

[3] O. S. Bushuyev *et al.*, "What Should We Make with CO2 and How Can We Make It?," *Joule,* vol. 2, no. 5, pp. 825-832, 2018-05-01 2018, doi: 10.1016/j.joule.2017.09.003.

[4] T. N. Nguyen and C. T. Dinh, "Gas diffusion electrode design for electrochemical carbon dioxide reduction," *Chem Soc Rev,* vol. 49, no. 21, pp. 7488-7504, Nov 7 2020, doi: 10.1039/d0cs00230e.

[5] H. Shin, K. U. Hansen, and F. Jiao, "Techno-economic assessment of low-temperature carbon dioxide electrolysis," *Nature Sustainability,* vol. 4, no. 10, pp. 911-919, 2021-10-01 2021, doi: 10.1038/s41893-021-00739-x.

[6] M. G. Kibria *et al.*, "Electrochemical CO2 Reduction into Chemical Feedstocks: From Mechanistic Electrocatalysis Models to System Design," *Adv Mater,* vol. 31, no. 31, p. e1807166, Aug 2019, doi: 10.1002/adma.201807166.

[7] F. P. Garcia de Arquer *et al.*, "CO2 electrolysis to multicarbon products at activities greater than 1 A cm(-2)," (in en), *Science,* vol. 367, no. 6478, pp. 661-666, Feb 7 2020, doi: 10.1126/science.aay4217.

[8] R. I. Masel *et al.*, "An industrial perspective on catalysts for low-temperature CO2 electrolysis," (in en), *Nat Nanotechnol,* vol. 16, no. 2, pp. 118-128, Feb 2021, doi: 10.1038/s41565-020-00823-x.

[9] T. K. Todorova, M. W. Schreiber, and M. Fontecave, "Mechanistic Understanding of CO2 Reduction Reaction (CO2RR) Toward Multicarbon Products by Heterogeneous Copper-Based Catalysts," *ACS Catalysis,* vol. 10, no. 3, pp. 1754-1768, 2020-02-07 2019, doi: 10.1021/acscatal.9b04746.

[10] J. D. Goodpaster, A. T. Bell, and M. Head-Gordon, "Identification of Possible Pathways for C-C Bond Formation during Electrochemical Reduction of CO2: New Theoretical Insights from an Improved Electrochemical Model," *J Phys Chem Lett,* vol. 7, no. 8, pp. 1471-7, Apr 21 2016, doi: 10.1021/acs.jpclett.6b00358.

[11] G. Liu *et al.*, "CO2 reduction on pure Cu produces only H2 after subsurface O is depleted: Theory and experiment," *Proc Natl Acad Sci U S A,* vol. 118, no. 23, p. e2012649118, Jun 8 2021, doi: 10.1073/pnas.2012649118.

[12] D. Zhong *et al.*, "Coupling of Cu(100) and (110) Facets Promotes Carbon Dioxide Conversion to Hydrocarbons and Alcohols," *Angew Chem Int Ed Engl,* vol. 60, no. 9, pp. 4879-4885, Feb 23 2021, doi: 10.1002/anie.202015159.

[13] H. Li *et al.*, "High-Rate CO2 Electroreduction to C2+ Products over a Copper-Copper Iodide Catalyst," (in en), *Angew Chem Int Ed Engl,* vol. 60, no. 26, pp. 14329-14333, Jun 21 2021, doi: 10.1002/anie.202102657.

[14] C. Chen *et al.*, "The in situ study of surface species and structures of oxide-derived copper catalysts for electrochemical CO2 reduction," *Chem Sci,* vol. 12, no. 16, pp. 5938-5943, Apr 28 2021, doi: 10.1039/d1sc00042j.
[15] P. Wang *et al.*, "Synergized Cu/Pb Core/Shell Electrocatalyst for High-Efficiency CO2 Reduction to C2+ Liquids," *ACS Nano,* vol. 15, no. 1, pp. 1039-1047, Jan 26 2021, doi: 10.1021/acsnano.0c07869.
[16] L. Xiong *et al.*, "Breaking the Linear Scaling Relationship by Compositional and Structural Crafting of Ternary Cu-Au/Ag Nanoframes for Electrocatalytic Ethylene Production," (in en), *Angew Chem Int Ed Engl,* vol. 60, no. 5, pp. 2508-2518, Feb 1 2021, doi: 10.1002/anie.202012631.
[17] S. Sultan *et al.*, "Interface rich CuO/Al2CuO4 surface for selective ethylene production from electrochemical CO2 conversion," *Energ Environ Sci,* vol. 15, no. 6, pp. 2397-2409, 2022, doi: 10.1039/d1ee03861c.
[18] Y. Yan *et al.*, "Ultrathin CuNi Nanosheets for CO2 Reduction and O2 Reduction Reaction in Fuel Cells," *Acs Mater Lett,* vol. 3, no. 8, pp. 1143-1150, 2021, doi: 10.1021/acsmaterialslett.1c00351.
[19] C. Peng *et al.*, "Lithiation-Enabled High-Density Nitrogen Vacancies Electrocatalyze CO2 to C2 Products," *Adv Mater,* vol. 33, no. 40, p. e2103150, Oct 2021, doi: 10.1002/adma.202103150.
[20] X. Yan *et al.*, "Boosting CO2 electroreduction to C2+ products on fluorine-doped copper," *Green Chemistry,* vol. 24, no. 5, pp. 1989-1994, 2022-01-01 2022, doi: 10.1039/d1gc04824d.
[21] C. F. Wen *et al.*, "Highly Ethylene-Selective Electrocatalytic CO2 Reduction Enabled by Isolated Cu-S Motifs in Metal-Organic Framework Based Precatalysts," *Angew Chem Int Ed Engl,* vol. 61, no. 2, p. e202111700, Jan 10 2022, doi: 10.1002/anie.202111700.
[22] R. Wang, J. Liu, Q. Huang, L. Z. Dong, S. L. Li, and Y. Q. Lan, "Partial Coordination-Perturbed Bi-Copper Sites for Selective Electroreduction of CO2 to Hydrocarbons," *Angew Chem Int Ed Engl,* vol. 60, no. 36, pp. 19829-19835, Sep 1 2021, doi: 10.1002/anie.202105343.
[23] X. Wang *et al.*, "Efficient electrically powered CO2-to-ethanol via suppression of deoxygenation," *Nature Energy,* vol. 5, no. 6, pp. 478-486, 2020-06-01 2020, doi: 10.1038/s41560-020-0607-8.
[24] C. Chen *et al.*, "Cu-Ag Tandem Catalysts for High-Rate CO2 Electrolysis toward Multicarbons," *Joule,* vol. 4, no. 8, pp. 1688-1699, 2020, doi: 10.1016/j.joule.2020.07.009.
[25] E. P. George, D. Raabe, and R. O. Ritchie, "High-entropy alloys," *Nature Reviews Materials,* vol. 4, no. 8, pp. 515-534, 2019-08-01 2019, doi: 10.1038/s41578-019-0121-4.
[26] J. W. Yeh *et al.*, "Nanostructured High-Entropy Alloys with Multiple Principal Elements: Novel Alloy Design Concepts and Outcomes," *Advanced Engineering Materials,* vol. 6, no. 5, pp. 299-303, 2004, doi: 10.1002/adem.200300567.
[27] B. Wang, Y. Yao, X. Yu, C. Wang, C. Wu, and Z. Zou, "Understanding the enhanced catalytic activity of high entropy alloys: from theory to experiment," *Journal of Materials Chemistry A,* vol. 9, no. 35, pp. 19410-19438, 2021, doi: 10.1039/d1ta02718b.
[28] K. Chen *et al.*, "Enhancing ORR/OER active sites through lattice distortion of Fe-enriched FeNi3 intermetallic nanoparticles doped N-doped carbon for high-performance

rechargeable Zn-air battery," *J Colloid Interface Sci,* vol. 582, no. Pt B, pp. 977-990, Jan 15 2021, doi: 10.1016/j.jcis.2020.08.101.

[29] T. Scientific. "Transmission Electron Microscopy vs Scanning Electron Microscopy." ThermoFisher Scientific. https://www.thermofisher.com/ca/en/home/materials-science/learning-center/applications/sem-tem-difference.html (accessed.

[30] T. Scientific. "Inductively Coupled Plasma Mass Spectrometry (ICP-MS) Information." ThermoFisher Scientific. https://www.thermofisher.com/ca/en/home/industrial/spectroscopy-elemental-isotope-analysis/spectroscopy-elemental-isotope-analysis-learning-center/trace-elemental-analysis-tea-information/inductively-coupled-plasma-mass-spectrometry-icp-ms-information.html (accessed.

[31] T. Scientific. "X-Ray Photoelectron Spectroscopy." ThermoFisher Scientific. https://www.thermofisher.com/ca/en/home/materials-science/xps-technology.html (accessed.

[32] T. Paraskova. "U.S. Natural Gas Price Jumps Above $6." oilprice.com. https://oilprice.com/Energy/Gas-Prices/US-Natural-Gas-Price-Jumps-Above-6.html (accessed.

[33] U. S. E. I. Administration. "Energy conversion calculators: NATURAL GAS CONVERSION CALCULATOR." https://www.eia.gov/energyexplained/units-and-calculators/energy-conversion-calculators.php#natgascalc (accessed 2022).

[34] OpenStax, *Chemistry*: OpenStax CNX, 2016. [Online]. Available: http://cnx.org/contents/85abf193-2bd2-4908-8563-90b8a7ac8df6@9.311. Accessed on: 2022.

[35] E. W. Lees *et al.*, "Electrodes Designed for Converting Bicarbonate into CO," *ACS Energy Letters,* vol. 5, no. 7, pp. 2165-2173, 2020-07-10 2020, doi: 10.1021/acsenergylett.0c00898.

[36] R. K. Miao *et al.*, "Electroosmotic flow steers neutral products and enables concentrated ethanol electroproduction from CO2," *Joule,* vol. 5, no. 10, pp. 2742-2753, 2021, doi: 10.1016/j.joule.2021.08.013.

[37] J. Sisler *et al.*, "Ethylene Electrosynthesis: A Comparative Techno-economic Analysis of Alkaline vs Membrane Electrode Assembly vs CO2–CO–C2H4 Tandems," *ACS Energy Letters,* vol. 6, no. 3, pp. 997-1002, 2021-03-12 2021, doi: 10.1021/acsenergylett.0c02633.

[38] R. P. Putra, H. Horino, and I. I. Rzeznicka, "An Efficient Electrocatalyst for Oxygen Evolution Reaction in Alkaline Solutions Derived from a Copper Chelate Polymer via In Situ Electrochemical Transformation," *Catalysts,* vol. 10, no. 2, p. 233, 2020-02-15 2020, doi: 10.3390/catal10020233.

[39] A. K. Ummireddi, S. K. Sharma, and R. G. S. Pala, "Inhibition of hydrogen evolution without debilitating electrochemical CO2 reduction via the local suppression of proton concentration and blocking of step-edges by pyridine functionalization on Cu electrocatalysts," *Catalysis Science & Technology,* vol. 11, no. 14, pp. 4857-4865, 2021, doi: 10.1039/d1cy00712b.

[40] R. Urban. "Electricity Prices in Canada 2021." https://www.energyhub.org/electricity-prices/ (accessed 2022).

[41] S. E. T. Office, "2030 Solar Cost Targets," 2021. [Online]. Available: https://www.energy.gov/eere/solar/articles/2030-solar-cost-targets

[42] C. Song *et al.*, "Tri-reforming of Methane over Ni Catalysts for CO2 Conversion to Syngas With Desired H2/CO Ratios Using Flue Gas of Power Plants Without CO2 Separation," in *Carbon Dioxide Utilization for Global Sustainability, Proceedings of 7ththe International Conference on Carbon Dioxide Utilization*, vol. 153, (Studies in Surface Science and Catalysis: Elsevier Science & Technology, 2004, pp. 315-322.

[43] Y. Xu *et al.*, "Oxygen-tolerant electroproduction of C2 products from simulated flue gas," *Energ Environ Sci,* vol. 13, no. 2, pp. 554-561, 2020, doi: 10.1039/c9ee03077h.

[44] D. W. Keith, G. Holmes, D. St. Angelo, and K. Heidel, "A Process for Capturing CO2 from the Atmosphere," *Joule,* vol. 2, no. 8, pp. 1573-1594, 2018-08-01 2018, doi: 10.1016/j.joule.2018.05.006.

[45] J. E. Huang *et al.*, "CO2 electrolysis to multicarbon products in strong acid," *Science,* vol. 372, no. 6546, pp. 1074-1078, Jun 4 2021, doi: 10.1126/science.abg6582.

[46] C. P. O'Brien *et al.*, "Single Pass CO2 Conversion Exceeding 85% in the Electrosynthesis of Multicarbon Products via Local CO2 Regeneration," *ACS Energy Letters,* vol. 6, no. 8, pp. 2952-2959, 2021-08-13 2021, doi: 10.1021/acsenergylett.1c01122.

[47] C. f. C. a. E. Solutions. "California Cap and Trade." https://www.c2es.org/content/california-cap-and-trade/ (accessed 2022).

[48] D. Materials. "Electrolyzer Hardware." Dioxide Materials https://dioxidematerials.com/product-category/electrolyzer_kits/electrolyzer-hardware/ (accessed 2022).

[49] C. Energy. "Natural Gas and Electricity." CenterPoint Energy. https://www.centerpointenergy.com/en-us/Services/Pages/natural-gas-electricity-cost-comparison.aspx (accessed 2022).

[50] M. Institute. "METHANOL PRICE AND SUPPLY/DEMAND." Methanol Institute. https://www.methanol.org/methanol-price-supply-demand/ (accessed April, 2022).

[51] T. O. Cleanup. "THE OCEAN CLEANUP SUNGLASSES." The Ocean Cleanup. https://products.theoceancleanup.com/ (accessed 2022).

[52] Y. Y. Birdja, E. Perez-Gallent, M. C. Figueiredo, A. J. Gottle, F. Calle-Vallejo, and M. T. M. Koper, "Advances and challenges in understanding the electrocatalytic conversion of carbon dioxide to fuels," (in English), *Nat. Energy,* vol. 4, no. 9, pp. 732-745, Sep 2019, doi: 10.1038/s41560-019-0450-y.

[53] R. I. Masel *et al.*, "An industrial perspective on catalysts for low-temperature CO_2 electrolysis," (in English), *Nat. Nanotechnol.,* vol. 16, no. 2, pp. 118-128, Feb 2021, doi: 10.1038/s41565-020-00823-x.

[54] S. Jin, Z. M. Hao, K. Zhang, Z. H. Yan, and J. Chen, "Advances and Challenges for the Electrochemical Reduction of CO_2 to CO: From Fundamentals to Industrialization," (in English), *Angew. Chem. Int. Edit.,* vol. 60, no. 38, pp. 20627-20648, Sep 13 2021, doi: 10.1002/anie.202101818.

[55] M. B. Ross *et al.*, "Designing materials for electrochemical carbon dioxide recycling," (in English), *Nat. Catal.,* vol. 2, no. 8, pp. 648-658, Aug 2019, doi: 10.1038/s41929-019-0306-7.

[56] Y. Zheng, A. Vasileff, X. L. Zhou, Y. Jiao, M. Jaroniec, and S. Z. Qiao, "Understanding the Roadmap for Electrochemical Reduction of CO_2 to Multi-Carbon Oxygenates and Hydrocarbons on Copper-Based Catalysts," (in English), *J. Am. Chem. Soc.,* vol. 141, no. 19, pp. 7646-7659, May 15 2019, doi: 10.1021/jacs.9b02124.

[57] C. Du, X. Wang, W. Chen, S. Feng, J. Wen, and Y. A. Wu, "CO2 transformation to multicarbon products by photocatalysis and electrocatalysis," (in en), *Materials Today Advances,* vol. 6, p. 100071, June 1, 2020 2020, doi: 10.1016/j.mtadv.2020.100071.

[58] M. Zhong *et al.*, "Accelerated discovery of CO_2 electrocatalysts using active machine learning," (in English), *Nature,* vol. 581, no. 7807, p. 178, May 2020, doi: 10.1038/s41586-020-2242-8.

[59] Y. Hori, A. Murata, and R. Takahashi, "Formation of Hydrocarbons in the Electrochemical Reduction of Carbon-Dioxide at a Copper Electrode in Aqueous-Solution," (in English), *J. Chem. Soc. Farad. T. I,* vol. 85, pp. 2309-2326, Aug 1989, doi: 10.1039/f19898502309.

[60] S. Nitopi *et al.*, "Progress and Perspectives of Electrochemical CO_2 Reduction on Copper in Aqueous Electrolyte," (in English), *Chem. Rev.,* vol. 119, no. 12, pp. 7610-7672, Jun 26 2019, doi: 10.1021/acs.chemrev.8b00705.

[61] A. A. Peterson, F. Abild-Pedersen, F. Studt, J. Rossmeisl, and J. K. Norskov, "How copper catalyzes the electroreduction of carbon dioxide into hydrocarbon fuels," (in English), *Energ. Environ. Sci.,* vol. 3, no. 9, pp. 1311-1315, Sep 2010, doi: 10.1039/c0ee00071j.

[62] A. J. Garza, A. T. Bell, and M. Head-Gordon, "Mechanism of CO_2 Reduction at Copper Surfaces: Pathways to C_2 Products," (in English), *ACS Catal.,* vol. 8, no. 2, pp. 1490-1499, Feb 2018, doi: 10.1021/acscatal.7b03477.

[63] M. Ma, K. Djanashvili, and W. A. Smith, "Controllable Hydrocarbon Formation from the Electrochemical Reduction of CO_2 over Cu Nanowire Arrays," (in English), *Angew. Chem. Int. Edit.,* vol. 55, no. 23, pp. 6680-6684, Jun 1 2016, doi: 10.1002/anie.201601282.

[64] C. W. Lee *et al.*, "Defining a Materials Database for the Design of Copper Binary Alloy Catalysts for Electrochemical CO_2 Conversion," (in English), *Adv. Mater.,* vol. 30, no. 42, p. 1704717, Oct 18 2018, doi: 10.1002/adma.201704717.

[65] Y. S. Zhou *et al.*, "Dopant-induced electron localization drives CO_2 reduction to C_2 hydrocarbons," (in English), *Nat. Chem.,* vol. 10, no. 9, pp. 974-980, Sep 2018, doi: 10.1038/s41557-018-0092-x.

[66] F. W. Li *et al.*, "Molecular tuning of CO_2-to-ethylene conversion," (in English), *Nature,* vol. 577, no. 7791, p. 509, Jan 2020, doi: 10.1038/s41586-019-1782-2.

[67] S. Ma *et al.*, "Electroreduction of Carbon Dioxide to Hydrocarbons Using Bimetallic Cu-Pd Catalysts with Different Mixing Patterns," (in English), *J. Am. Chem. Soc.,* vol. 139, no. 1, pp. 47-50, Jan 11 2017, doi: 10.1021/jacs.6b10740.

[68] P. B. O'Mara *et al.*, "Cascade Reactions in Nanozymes: Spatially Separated Active Sites inside Ag-Core-Porous-Cu-Shell Nanoparticles for Multistep Carbon Dioxide Reduction to Higher Organic Molecules," (in English), *J. Am. Chem. Soc.,* vol. 141, no. 36, pp. 14093-14097, Sep 11 2019, doi: 10.1021/jacs.9b07310.

[69] C. B. Chen *et al.*, "Cu-Ag Tandem Catalysts for High-Rate CO_2 Electrolysis toward Multicarbons," (in English), *Joule,* vol. 4, no. 8, pp. 1688-1699, Aug 19 2020, doi: 10.1016/j.joule.2020.07.009.

[70] T. Y. Zhang, J. C. Bui, Z. Y. Li, A. T. Bell, A. Z. Weber, and J. J. Wu, "Highly selective and productive reduction of carbon dioxide to multicarbon products via in situ CO management using segmented tandem electrodes," (in English), *Nat. Catal.,* vol. 5, pp. 202-211, Mar 3 2022, doi: 10.1038/s41929-022-00751-0.

[71] J. Li *et al.*, "Constraining CO coverage on copper promotes high-efficiency ethylene electroproduction," (in English), *Nat. Catal.,* vol. 2, no. 12, pp. 1124-1131, Dec 2019, doi: 10.1038/s41929-019-0380-x.

[72] M. C. Biesinger, L. W. M. Lau, A. R. Gerson, and R. S. C. Smart, "Resolving surface chemical states in XPS analysis of first row transition metals, oxides and hydroxides: Sc, Ti, V, Cu and Zn," (in English), *Appl. Surf. Sci.,* vol. 257, no. 3, pp. 887-898, Nov 15 2010, doi: 10.1016/j.apsusc.2010.07.086.

[73] C. Du, S. J. He, M. M. Liu, X. H. Gao, R. Z. Zhang, and W. Chen, "Novel $Pd_{13}Cu_3S_7$ nanotubes with high electrocatalytic activity towards both oxygen reduction and ethanol oxidation reactions," (in English), *CrystEngComm,* vol. 18, no. 32, pp. 6055-6061, 2016, doi: 10.1039/c6ce00688d.

[74] S. H. Lee *et al.*, "Oxidation State and Surface Reconstruction of Cu under CO_2 Reduction Conditions from In Situ X-ray Characterization," (in English), *J. Am. Chem. Soc.,* vol. 143, no. 2, pp. 588-592, Jan 20 2021, doi: 10.1021/jacs.0c10017.

[75] Y. Xu *et al.*, "Self-Cleaning CO_2 Reduction Systems: Unsteady Electrochemical Forcing Enables Stability," (in English), *ACS Energy Lett.,* vol. 6, no. 2, pp. 809-815, Feb 12 2021, doi: 10.1021/acsenergylett.0c02401.

[76] F. Calle-Vallejo and M. T. M. Koper, "Theoretical Considerations on the Electroreduction of CO to C_2 Species on Cu(100) Electrodes," (in English), *Angew. Chem. Int. Edit.,* vol. 52, no. 28, pp. 7282-7285, Jul 8 2013, doi: 10.1002/anie.201301470.

[77] Y. W. Lum, T. Cheng, W. A. Goddard, and J. W. Ager, "Electrochemical CO Reduction Builds Solvent Water into Oxygenate Products," (in English), *J. Am. Chem. Soc.,* vol. 140, no. 30, pp. 9337-9340, Aug 1 2018, doi: 10.1021/jacs.8b03986.

[78] Y. G. C. Li *et al.*, "Binding Site Diversity Promotes CO_2 Electroreduction to Ethanol," (in English), *J. Am. Chem. Soc.,* vol. 141, no. 21, pp. 8584-8591, May 29 2019, doi: 10.1021/jacs.9b02945.

[79] T. K. Todorova, M. W. Schreiber, and M. Fontecave, "Mechanistic Understanding of CO_2 Reduction Reaction (CO_2RR) Toward Multicarbon Products by Heterogeneous Copper-Based Catalysts," (in English), *ACS Catal.,* vol. 10, no. 3, pp. 1754-1768, Feb 7 2020, doi: 10.1021/acscatal.9b04746.

[80] K. J. P. Schouten, Y. Kwon, C. J. M. van der Ham, Z. Qin, and M. T. M. Koper, "A new mechanism for the selectivity to C_1 and C_2 species in the electrochemical reduction of carbon dioxide on copper electrodes," (in English), *Chem. Sci.,* vol. 2, no. 10, pp. 1902-1909, 2011, doi: 10.1039/c1sc00277e.

[81] J. Santatiwongchai, K. Faungnawakij, and P. Hirunsit, "Comprehensive Mechanism of CO_2 Electroreduction toward Ethylene and Ethanol: The Solvent Effect from Explicit Water Cu(100) Interface Models," (in English), *ACS Catal.,* vol. 11, no. 15, pp. 9688-9701, Aug 6 2021, doi: 10.1021/acscatal.1c01486.

[82] H. Xiao, T. Cheng, W. A. Goddard, and R. Sundararaman, "Mechanistic Explanation of the pH Dependence and Onset Potentials for Hydrocarbon Products from Electrochemical

Reduction of CO on Cu (111)," (in English), *J. Am. Chem. Soc.,* vol. 138, no. 2, pp. 483-486, Jan 20 2016, doi: 10.1021/jacs.5b11390.

[83] J. H. Montoya, A. A. Peterson, and J. K. Norskov, "Insights into C-C Coupling in CO_2 Electroreduction on Copper Electrodes," (in English), *ChemCatChem,* vol. 5, no. 3, pp. 737-742, Mar 2013, doi: 10.1002/cctc.201200564.

[84] W. J. Luo, X. W. Nie, M. J. Janik, and A. Asthagiri, "Facet Dependence of CO_2 Reduction Paths on Cu Electrodes," (in English), *ACS Catal.,* vol. 6, no. 1, pp. 219-229, Jan 2016, doi: 10.1021/acscatal.5b01967.

[85] Y. Jia, F. Li, K. Fan, and L. Sun, "Cu-based bimetallic electrocatalysts for CO_2 reduction," *Adv. Powder Mater.,* vol. 1, no. 1, p. 100012, 2022/01/01/ 2022, doi: 10.1016/j.apmate.2021.10.003.

[86] J. K. Norskov, F. Abild-Pedersen, F. Studt, and T. Bligaard, "Density functional theory in surface chemistry and catalysis," (in English), *P. Natl. Acad. Sci. USA,* vol. 108, no. 3, pp. 937-943, Jan 18 2011, doi: 10.1073/pnas.1006652108.

[87] G. Kresse and J. Furthmuller, "Efficiency of ab-initio total energy calculations for metals and semiconductors using a plane-wave basis set," (in English), *Comp. Mater. Sci.,* vol. 6, no. 1, pp. 15-50, Jul 1996, doi: 10.1016/0927-0256(96)00008-0.

[88] J. P. Perdew, K. Burke, and M. Ernzerhof, "Generalized gradient approximation made simple," (in English), *Phys. Rev. Lett.,* vol. 77, no. 18, pp. 3865-3868, Oct 28 1996, doi: 10.1103/PhysRevLett.77.3865.

[89] G. Kresse and D. Joubert, "From ultrasoft pseudopotentials to the projector augmented-wave method," (in English), *Phys. Rev. B,* vol. 59, no. 3, pp. 1758-1775, Jan 15 1999, doi: 10.1103/PhysRevB.59.1758.

[90] H. J. Monkhorst and J. D. Pack, "Special Points for Brillouin-Zone Integrations," (in English), *Phys. Rev. B,* vol. 13, no. 12, pp. 5188-5192, 1976, doi: 10.1103/PhysRevB.13.5188.

[91] P. E. Blochl, O. Jepsen, and O. K. Andersen, "Improved Tetrahedron Method for Brillouin-Zone Integrations," (in English), *Phys. Rev. B,* vol. 49, no. 23, pp. 16223-16233, Jun 15 1994, doi: 10.1103/PhysRevB.49.16223.

[92] S. Grimme, J. Antony, S. Ehrlich, and H. Krieg, "A consistent and accurate ab initio parametrization of density functional dispersion correction (DFT-D) for the 94 elements H-Pu," (in English), *J. Chem. Phys.,* vol. 132, no. 15, p. 154104, Apr 21 2010, doi: 10.1063/1.3382344.

[93] P. N. Plessow, "Efficient Transition State Optimization of Periodic Structures through Automated Relaxed Potential Energy Surface Scans," (in English), *J. Chem. Theory Comput.,* vol. 14, no. 2, pp. 981-990, Feb 2018, doi: 10.1021/acs.jctc.7b01070.

[94] J. K. Norskov *et al.*, "Origin of the overpotential for oxygen reduction at a fuel-cell cathode," (in English), *J. Phys. Chem. B,* vol. 108, no. 46, pp. 17886-17892, Nov 18 2004, doi: 10.1021/jp047349j.

[95] S. Pérez-Rodríguez, E. Pastor, and M. J. Lázaro, "Electrochemical behavior of the carbon black Vulcan XC-72R: Influence of the surface chemistry," *International Journal of Hydrogen Energy,* vol. 43, no. 16, pp. 7911-7922, 2018, doi: 10.1016/j.ijhydene.2018.03.040.

[96] Y. Yao *et al.*, "Carbothermal shock synthesis of high-entropy-alloy nanoparticles," *Science,* vol. 359, no. 6383, pp. 1489-1494, Mar 30 2018, doi: 10.1126/science.aan5412.

[97] J. P. Mills, C. Du, Z. Chen, T. Guo, and Y. A. Wu, "Catalyst design strategies for aqueous N2 electroreduction," *Applied Materials Today,* vol. 25, p. 101184, 2021-12-01 2021, doi: 10.1016/j.apmt.2021.101184.

[98] T. Li, E. W. Lees, Z. Zhang, and C. P. Berlinguette, "Conversion of Bicarbonate to Formate in an Electrochemical Flow Reactor," (in en), *ACS Energy Letters,* vol. 5, no. 8, pp. 2624-2630, 2020-08-14 2020, doi: 10.1021/acsenergylett.0c01291.